The Astrophysical Journal, 751:102 (25pp), 2012 June 1 doi:10.1088/0004-637X/751/2/102

NUCLEOSYNTHESIS AND THE INHOMOGENEOUS CHEMICAL EVOLUTION OF THE CARINA DWARF GALAXY*

Kim A. Venn[1], Matthew D. Shetrone[2], Mike J. Irwin[3], Vanessa Hill[4,5], Pascale Jablonka[5,6], Eline Tolstoy[7], Bertrand Lemasle[7], Mike Divell[1], Else Starkenburg[7], Bruno Letarte[8], Charles Baldner[9], Giuseppina Battaglia[10], Amina Helmi[7], Andreas Kaufer[11], and Francesca Primas[10]

[1] Department of Physics and Astronomy, University of Victoria, 3800 Finnerty Road, Victoria, BC V8P 1A1, Canada; kvenn@uvic.ca
[2] McDonald Observatory, University of Texas at Austin, HC75 Box 1337-McD, Fort Davis, TX 79734, USA
[3] Institute of Astronomy, University of Cambridge, Madingley Road, Cambridge CB03 0HA, UK
[4] Laboratoire Cassiopée UMR 6202, Université de Nice Sophia-Antipolis, CNRS, Observatoire de la Côte d'Azur, France
[5] GEPI, Observatoire de Paris, CNRS UMR 8111, Université Paris Diderot, F-92125, Meudon, Cedex, France
[6] Laboratoire d'Astrophysique, École Polytechnique Fédérale de Lausanne (EPFL), 1290 Sauverny, Switzerland
[7] Kapteyn Astronomical Institute, University of Groningen, P.O. Box 800, 9700 AV Groningen, The Netherlands
[8] South African Astronomical Observatory, Observatory Road, 7935 Observatory, South Africa
[9] Department of Astronomy, Yale University, P.O. Box 208101, New Haven, CT 06520-8101, USA
[10] European Southern Observatory, Karl-Schwarzschild-Strasse 2, 85748 Garching, Germany
[11] European Southern Observatory, Alonso de Cordova 3107, Santiago, Chile
Received 2011 August 24; accepted 2012 March 23; published 2012 May 10

ABSTRACT

The detailed abundances of 23 chemical elements in nine bright red giant branch stars in the Carina dwarf spheroidal galaxy are presented based on high-resolution spectra gathered at the Very Large Telescope (VLT) and Magellan telescopes. A spherical model atmospheres analysis is applied using standard methods (local thermodynamic equilibrium and plane-parallel radiative transfer) to spectra ranging from 380 to 680 nm. Stellar parameters are found to be consistent between photometric and spectroscopic analyses, both at moderate and high resolution. The stars in this analysis range in metallicity from $-2.9 < [Fe/H] < -1.3$, and adopting the ages determined by Lemasle et al., we are able to examine the chemical evolution of Carina's old and intermediate-aged populations. One of the main results from this work is the evidence for inhomogeneous mixing in Carina and therefore for a poor statistical sampling of the supernova contributions when forming stars; a large dispersion in [Mg/Fe] indicates poor mixing in the old population, an offset in the [α/Fe] ratios between the old and intermediate-aged populations (when examined with previously published results) suggests that the second star formation event occurred in α-enriched gas, and one star, Car-612, seems to have formed in a pocket enhanced in SN Ia/II products. This latter star provides the first direct link between the formation of stars with enhanced SN Ia/II ratios in dwarf galaxies to those found in the outer Galactic halo (Ivans et al.). Another important result is the potential evidence for SN II driven winds. We show that the very metal-poor stars in Carina have not been enhanced in asymptotic giant branch or SN Ia products, and therefore their very low ratios of [Sr/Ba] suggests the loss of contributions from the early SNe II. Low ratios of [Na/Fe], [Mn/Fe], and [Cr/Fe] in two of these stars support this scenario, with additional evidence from the low [Zn/Fe] upper limit for one star. It is interesting that the chemistry of the metal-poor stars in Carina is not similar to those in the Galaxy, most of the other dwarf spheroidal galaxies, or the ultra faint dwarfs, and suggests that Carina may be at the critical mass where *some* chemical enrichments are lost through SN II driven winds.

Key words: galaxies: abundances – galaxies: dwarf – galaxies: evolution – galaxies: individual (Carina dwarf galaxy) – Local Group

Online-only material: color figures, machine-readable tables

1. INTRODUCTION

Chemical analyses of stars in nearby classical dwarf galaxies have swelled in the past decade, with the advent of large aperture telescopes, high-efficiency spectrographs, and multiplexing capabilities. Detailed abundances are now available for dozens to hundreds of stars in classical dwarf spheroidal galaxies (dSph), ultra faint dwarf (UFD) systems, and even a few massive stars in some low-mass dwarf irregular galaxies; see the review by Tolstoy et al. (2009). These chemical studies have shown that low-mass dwarf galaxies have had a slower chemical evolution than the stellar populations in the Milky Way. For example, the majority of stars in dSphs have mean metallicities and [α/Fe][12] ratios that are lower than those of the Sun. Stars in dwarf galaxies also tend to have different heavy element ratios (e.g., higher [Ba/Y] or [La/Eu]) than similar metallicity stars in the Galaxy (e.g., Venn et al. 2004; Aoki et al. 2009; Letarte et al. 2010). On the other hand, the most metal-poor stars in dwarf galaxies, with [Fe/H] $\leqslant -2.5$, tend to have similar abundance ratios to Galactic halo stars, even for the α and heavy element ratios (e.g., Sculptor, Fornax, and Sextans; Tafelmeyer et al. 2010). This is also true of the very metal-poor stars in the UFDs (e.g., Com Ber, Boötes I, and Leo IV; Norris et al. 2008, 2010a; Feltzing et al. 2009; Frebel et al. 2010b; Simon et al. 2010). One exception are the α and heavy element abundances for metal-poor stars in Sextans, which show both offsets and larger dispersions than the Galaxy and other dwarf galaxies (Aoki et al. 2009).

* This project is partially based on VLT FLAMES spectroscopic observations obtained at the European Southern Observatory, proposals 074.B-0415 and 076.B-0146, and partially based on MIKE spectra gathered at the 6.5 m Magellan Telescopes, in Chile.

[12] $[X/Fe] = \log(X/Fe)_* - \log(X/Fe)_\odot$.

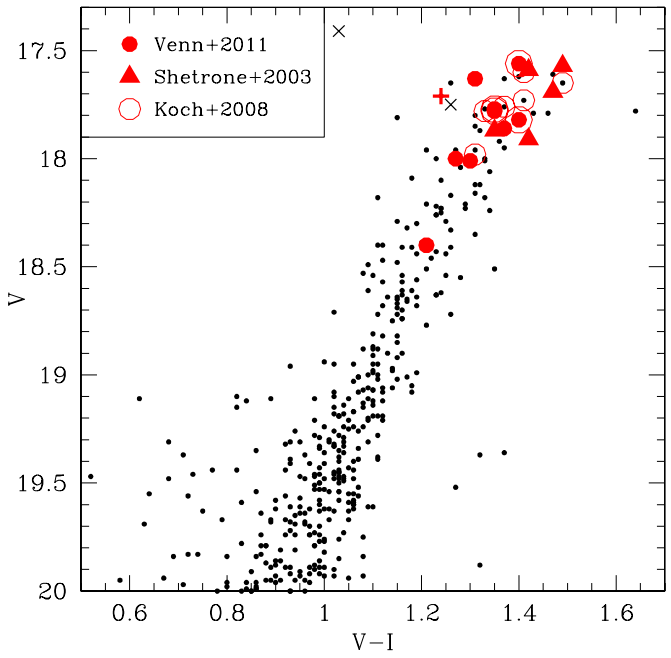

Figure 1. Color–magnitude diagram, V vs. $(V - I)$, for Carina from our ESO WFI data. Only stars with radial velocities >200 km s^{-1} (from Koch et al. 2006) are shown. Stars with high-resolution spectral analyses are identified by red symbols, including nine stars from this paper, five from Shetrone et al. (2003), and ten from Koch et al. (2008a; four are in common with this analysis). One carbon star is noted by the red cross, and two foreground objects are shown as black crosses. The faintest star in our sample is Car-7002.

(A color version of this figure is available in the online journal.)

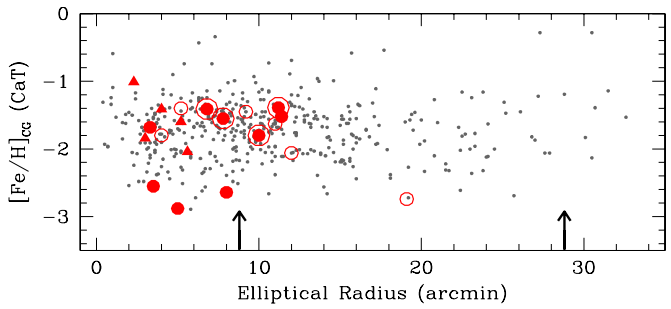

Figure 2. Spatial location and metallicities of the nine Carina stars in this paper, as well as five from Shetrone et al. (2003), and ten stars from Koch et al. (2008a; four are in common with this analysis). Symbols are the same as in Figure 1. These are compared to the distribution of 437 RGB stars from Koch et al. (2006), which have a high (3σ) probability of Carina membership. The metallicities on this plot are those determined by Koch et al. (2006). Elliptical radii are calculated using the structural parameters for Carina from Irwin & Hatzidimitriou (1995; central coordinates $6^h40.'6$ and $-50°56'$ for epoch B1950, position angle 65°, and ellipticity $\epsilon = 0.33$), and listed in Table 1, and core and tidal radii are indicated.

(A color version of this figure is available in the online journal.)

The Carina dwarf galaxy provides a new opportunity for chemical evolution and nucleosynthetic studies. It has a low mass that is similar to that of Sextans (Walker et al. 2009), and it has had an unusual, episodic star formation history. Its color–magnitude diagram (CMD) shows at least three main-sequence turnoffs (Monelli et al. 2003; Bono et al. 2010) and is best described by a star formation history with a well-defined old population (∼10–12 Gyr), a dominant intermediate-aged (IA) population (∼5–7 Gyr), and a trace young population (∼2 Gyr; although the specific timescales are uncertain). These star-forming episodes are separated by long quiescent periods, seen as gaps between the main-sequence turnoff points. It is estimated that 70%–80% of the stars in Carina have IAs, while most of the remaining stars are old and associated with the first star-forming episode (also see Dolphin 2002; Hernandez et al. 2000; Hurley-Keller et al. 1998; Mighell 1997). One wonders how this unique star formation history may have affected the chemical evolution of Carina.

In spite of its punctuated star formation history, Carina has an extremely narrow red giant branch (RGB). One possibly is that the RGB stars in Carina have a fortuitous alignment in the age–metallicity degeneracy, such that the older metal-poor stars overlay the metal enhanced IA stars. Alternatively, the narrow RGB could be dominated by IA stars only, if that population formed on a relatively short timescale and with only a modest metallicity spread (Rizzi et al. 2003; Bono et al. 2010). Low-resolution spectra of 437 RGB stars in Carina analyzed by Koch et al. (2006) showed the mean metallicity in Carina is [Fe/H] $\sim -1.7 \pm 0.9$, in agreement with similar analyses by Helmi et al. (2006) and Starkenburg et al. (2010). This metallicity spread is larger than predicted by Bono et al. (2010) from their CMD analysis (Δ[Fe/H] $\leqslant \pm 0.5$ dex). Koch et al. (2006) also found no significant gradients in metallicity or stellar population with position in Carina, unlike the results for Sculptor (Tolstoy et al. 2004) and Fornax (Battaglia et al. 2006).

High-resolution analyses of five RGB stars (Shetrone et al. 2003) and ten RGB stars (Koch et al. 2008a) supported the larger range in metallicity found by the low-resolution spectral analyses. These analyses also showed that Carina is like the other dSph galaxies in that the [α/Fe] ratios are lower than in Galactic halo stars with similar metallicity. Lanfranchi & Matteucci (2003, 2004) and Lanfranchi et al. (2006) used these data sets to develop chemical evolution models for Carina, tuning the high wind efficiency and low star formation efficiency to reproduce Carina's metallicity distribution function, [α/Fe] ratios, and low gas content.

In this paper, we present a new detailed abundance analysis of up to 23 elements in nine stars in the Carina dwarf galaxy. This work increases the number of elements, the number of stars, and the metallicity range previously explored. We also report the abundances for two newly discovered very metal-poor stars (with [Fe/H] ~ -2.85), which allow us to examine the earliest epoch of star formation. These results, with previously published abundances, are used to explore the unique star formation history and chemical evolution in Carina.

2. OBSERVATIONS AND DATA REDUCTIONS

The data presented in this paper were acquired at two observatories during separate time allocations in 2005 January. The FLAMES (Fibre Large Array Multi Element Spectrograph) multiobject spectrograph at the 8.2 m UT2 (Kueyen) at the Very Large Telescope (VLT) of the European Southern Observatory (ESO) was used to collect high-resolution spectra using both the UVES and GIRAFFE fiber modes (Pasquini et al. 2002). The analysis of the FLAMES/GIRAFFE spectra is presented by Lemasle et al. (2012). Also, the MIKE (Magellan Inamori Kyocera Echelle) spectrograph at the Magellan Landon 6.5 m Clay Telescope at the Las Campanas Observatory was used to collect high-resolution spectra of individual stars outside of the central field of Carina. Our targets and those previously analyzed with high-resolution spectral analyses by Koch et al. (2008a) and Shetrone et al. (2003) are shown in Figure 1 on the V versus $(V - I)$ CMD. These stars are also shown in Figure 2 as

Table 1
Observing Information

Star	Other Name	R.A. (2000)	Decl. (2000)	R_{ell} (arcmin)	Exp Time (s)	RV CaT (km s^{-1})	RV HR (km s^{-1})	S/N 4200	S/N 5200	S/N 6200
M68-6022	S195	12 39 17.0	−26 45 39	...	2 × 600	...	−95.1 ± 1.5	60	73	75
M68-6023	S239	12 39 37.6	−26 45 15	...	1 × 600	...	−94.8 ± 1.3	55	66	65
M68-6024	S225	12 39 30.1	−26 42 47	...	1 × 600	...	−96.2 ± 1.6	30	44	46
Car-1087	S12924 LGO4c-006621	6 41 15.4	−51 01 16	5.0	4 × 3600	229.3	220.1 ± 4.1	20	30	32
Car-5070	S24846 car1-t213	6 41 53.8	−50 58 11	3.5	3 × 3600	213.5	211.5 ± 3.5	20	30	32
Car-7002	S06496 LGO4c-000826 car0619-a2	6 40 49.1	−51 00 33	8.0	3 × 3600	226.6	224.2 ± 3.7	18	30	27
Car-484	car1-t057 (K) LGO4a-002181	6 41 39.6	−50 49 59	11.2	11 × 3600	232.6	229.4 ± 0.7	...	20	35
Car-524	car1-t083 LGO4a-002065	6 41 14.6	−50 51 10	11.4	11 × 3600	219.4	218.6 ± 0.7	...	20	40
Car-612	car1-t076 (K) LGO4a-001826	6 40 58.6	−50 53 35	10.0	11 × 3600	223.1	222.9 ± 0.7	...	19	29
Car-705	car1-t048 (K) LGO4a-001556	6 42 17.3	−50 55 55	6.8	11 × 3600	221.3	220.9 ± 0.9	...	18	28
Car-769	car1-t069 LGO4a-001364	6 41 19.7	−50 57 26	3.3	11 × 3600	219.4	218.9 ± 0.6	...	17	27
Car-1013	car1-t152 (K) LGO4c-006477	6 41 22.0	−51 03 43	7.8	11 × 3600	218.5	218.4 ± 1.5	...	11	15
Car-837	car1-t191 (C-star)	6 41 46.3	−50 58 56	...	11 × 3600	232.6	222.4 ± 0.7	...	20	30
Car-489	(non-member)	6 41 37.0	−50 50 07	...	11 × 3600	236.5	...	...	16	25
Car-X	(non-member)	6 41 26.9	−51 00 34	...	11 × 3600	...	4.9 ± 0.8	...	15	25

Notes. Data for M68 and the first three Carina stars are from the Magellan MIKE spectrograph, with the remaining nine Carina stars observed with the FLAMES spectrograph at the VLT. Stars partially analyzed by Koch et al. (2008a) are noted with "(K)" beside their alternative names. The S# target names are from P.B. Stetson's online database of homogeneous photometry (at http://cadcwww.hia.nrc.ca/stetson). Car-X is a bright target right next to Car-909, which was the actual target. S/N are the signal-to-noise ratios *per pixel*.

metallicity (from Koch et al. 2006) versus their location within Carina.

2.1. Magellan MIKE Spectra

Target selection for the Magellan run was from low-resolution spectra of the Ca II 8600 Å feature (=CaT) for hundreds of stars in the Carina dSph in the ESO archive (Koch et al. 2006; Helmi et al. 2006). The feature was used to ascertain membership from radial velocities, as well as estimate an initial metallicity for each target based on the CaT-metallicity calibration available at that time (Battaglia et al. 2008). Exposure times, radial velocities (km s^{-1}), the signal-to-noise ratio (S/N) at three wavelengths, the elliptical radius from the center of Carina (in arcminutes), and alternative names for the targets are summarized in Table 1. Spectra for three objects in the metal-poor globular cluster M68 were also taken as standard stars. M68 was chosen as a standard since it has low metallicity (Harris 1996) and low reddening. *BVI* magnitudes are from Stetson (2000, with corrections onto the Johnson-Kron–Cousins scale of the Landolt standard stars as in Stetson 2005), which places these stars on the upper RGB of M68 and suggests they have intrinsic luminosities similar to our program stars.

On the red side, the double echelle design covers 4850–9400 Å, and on the blue side, 3800–5050 Å. The quality of the blue spectra is significantly higher in the overlapping wavelength region (∼4850–5050 Å). Using a 1.″0 slit, a spectral resolution $R = 28{,}000$ (blue) to $R = 22{,}000$ (red) was obtained. The red chip had a gain of 1.0 electrons ADU^{-1} and read noise of four electrons; the blue chip had a gain of 0.47 electrons ADU^{-1} and a read noise of two electrons. We binned on-chip with 2 × 2 pixels. Table 1 lists the S/N per pixel achieved in the final combined spectra near 4200, 5200, and 6200 Å.

The data were reduced using standard IRAF[13] routines. Sky subtraction was done with a smooth fit perpendicular to the dispersion axis. Heliocentric corrections were applied to each spectrum before determining their radial velocities. Multiple spectra were median combined, which helped to remove cosmic ray strikes. Spectra taken of the Th–Ar lamp provided the wavelength calibration. Both quartz flats and screen flats were taken at varying exposure levels; no significant offsets were found between the well-illuminated quartz flats and the science exposures, thus the quartz flats were adopted for the data reductions. A small dark current was noticed on one corner of the blue chip in a region that did not receive starlight and therefore did not affect this analysis. The final spectra were normalized using *k*-sigma clipping with a nonlinear filter (a combination of a median and a boxcar). The effective scale length of the filter was set from 8 to 15 Å, dependent on the crowding of the spectral lines, and we found that this was sufficient to follow the continuum without affecting the presence of the lines when used in conjunction with iterative clipping. This method was also used by Battaglia et al. (2008) to normalize CaT spectra.

[13] IRAF is distributed by the National Optical Astronomy Observatory, which is operated by the Association of Universities for Research in Astronomy, Inc., under cooperative agreement with the National Science Foundation.

Table 2
Line List

Wave (Å)	χ (eV)	log gf	CAR 484	CAR 524	CAR 612	CAR 705	CAR 769	CAR 1013
Fe I								
5001.864	3.88	0.010	124.9	116.7	124.0	134.0	104.3	165.1
5006.120	2.83	−0.615	194.7	166.1	185.2	193.8	158.2	...
5012.070	0.86	−2.642	...	195.0	...	...	179.3	...
5014.940	3.94	−0.300	113.4	103.4	117.0	114.3	65.4	97.2

Notes. Equivalent widths are in mÅ and upper limits are noted. When spectrum syntheses have been used in the abundance analysis, then an "S" is noted.

(This table is available in its entirety in a machine-readable form in the online journal. A portion is shown here for guidance regarding its form and content.)

Table 3
MIKE Line List

Wave	χ	log gf	N6022	N6023	N6024	1087	5070	7002
Fe I								
5001.864	3.88	0.010	51.9	49.9	52.6	...	...	...
5006.120	2.83	−0.615	83.5	84.1	75.8	...	...	70.8
5012.070	0.86	−2.642	122.4	117.0	121.3	138.0	184.5	134.1
5014.940	3.94	−0.300	35.3	38.2	42.2	...	...	...

Notes. Equivalent widths are in mÅ and upper limits are noted. When spectrum syntheses have been used in the abundance analysis, then an "S" is noted.

(This table is available in its entirety in a machine-readable form in the online journal. A portion is shown here for guidance regarding its form and content.)

2.2. VLT FLAMES/UVES Data

Observations with the multi-object FLAMES spectrograph at the UT2 Kueyen ESO-VLT (Pasquini et al. 2002) were carried out for nine targets in the central region of Carina. In two separate configurations, the FLAMES/UVES fibers were placed on bright RGB stars resulting in nine stellar spectra and two sky observations. Two of the nine targets proved to be foreground RGB stars, while one is a carbon star that is unsuitable for our analysis. Target coordinates, exposure times, radial velocities (km s^{-1}), elliptical radius from the center of Carina (in arcmins), and the S/N at two wavelengths for the final combined spectra are listed in Table 1. Other names for each target are also listed. FLAMES/GIRAFFE spectra were simultaneously obtained at high resolution ($R = 20{,}000$) for 36 more stars in Carina, but over much shorter wavelength regions (three wavelength settings that yielded ∼250 Å each)—these are presented in a separate paper by Lemasle et al. (2012). Due to variable weather conditions, only 11 of the 1 hr exposures had sufficient signal to be used further in this analysis.

On the red side, the double echelle design covers 5840–6815 Å, and on the blue, 4800–5760 Å. A 1.″0 slit yields a spectral resolution $R = 47{,}000$. Table 1 lists the exposure times and S/N per pixel in the final combined spectra near 5200 and 6200 Å. Unfortunately, six of the 1 hr exposures did not have enough signal in the FLAMES/UVES fibers to be useful in this analysis. The data were reduced using the ESO FLAMES pipeline.[14] The sky spectrum was fit with a smoothly varying function, and this was subtracted from the stellar exposures per wavelength set up (to reduce adding more noise in already low S/N spectra). Each spectrum was then heliocentric velocity corrected, radial velocities were determined, and the spectra were co-added (weighted by the S/N). The final spectra were normalized using an iterative asymmetric k-sigma clipping routine with a nonlinear filter (like for the Magellan/MIKE spectra).

3. STELLAR ANALYSES

3.1. Line List

A range of elements are detectable in our spectra, which enables a comprehensive abundance analysis. Atomic lines for this analysis were selected from the literature, including the line lists from Shetrone et al. (2003), Cayrel et al. (2004), Aoki et al. (2007), Cohen et al. (2008), Letarte et al. (2009), Tafelmeyer et al. (2010), and Frebel et al. (2010b); see Tables 2 and 3. Atomic data for the Fe I lines were updated from O'Brian et al. (1991) when available, or the atomic data were updated to the latest values in the National Institute of Standards and Technology (NIST) database.[15]

3.2. Equivalent Width Measurements

Most of the elemental abundances in this analysis are determined from equivalent width (EW) measurements. Spectrum syntheses were used only for lines affected by hyperfine splitting or for elements with line measurements from low S/N spectra.

EWs were measured using the Gaussian fitting routine DAOSPEC (Stetson & Pancino 2008). The placement of the continuum is a critical step, as it influences the measurements of the EWs; thus some care was taken in assigning and testing the DAOSPEC fitting parameters. For example, a low-order polynomial (order 13) was adopted to allow DAOSPEC to measure the effective continuum, and tests of other low-order values (order =5 and =1) resulted in nearly identical EWs, with $\Delta EW < 1\%$. As a final exercise, the continuum was set to one so that DAOSPEC would not relocate the global continuum for the measurement (order = −1). Results from this test showed a slight offset $\leqslant +12\%$ in the EW measurements, as expected. We note this offset is similar to or less than our adopted EW measurement errors from the Cayrel formula (described below). For testing purposes, EWs were also measured with *splot* in IRAF to determine the area under the continuum. A comparison of these measurements with those from DAOSPEC for two of the stars observed with the MIKE spectrograph are shown in Figure 3.

The expected *minimum* measurement uncertainties on the equivalent widths (EW_{rms}) have been estimated using a revised Cayrel formula, i.e., a new derivation of the measurement errors on the EWs was presented by Battaglia et al. (2008), where it was found that the factor of 1.5 in the Cayrel (1988) formula is actually within the square root; thus,

$$EW_{rms} = (S/N)^{-1} \times \sqrt{1.5 \times FWHM \times \delta x},$$

where S/N is the signal-to-noise ratio per pixel, FWHM is the line full width at half-maximum, and δx is the pixel size. An extra 10% of the EW was added to this for a more conservative measurement error, such that

$$\Delta EW = EW_{rms} + 0.10 \times EW.$$

For the M68 stellar spectra taken at Magellan the revised Cayrel formula gives $EW_{rms} = 3$ mÅ, but $EW_{rms} = 6$ mÅ for the lower S/N spectra of the Carina stars observed with MIKE.

[14] The GIRAFFE Base-Line Data Reduction, girBLDRS, was written at the Observatory of Geneva by A. Blecha and G. Simond, and is available through SourceForge at http://girbldrs.sourceforge.net/.

[15] http://physics.nist.gov/PhysRefData/ASD/index.html

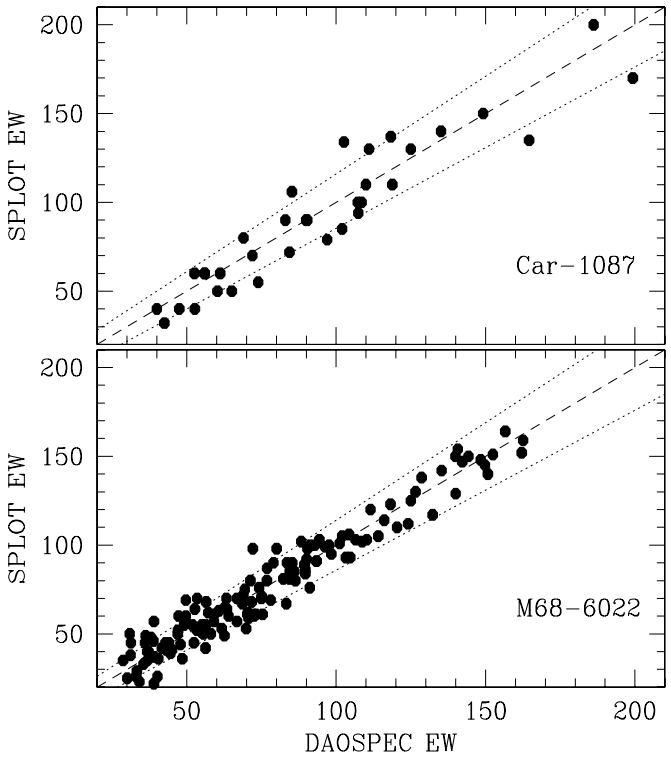

Figure 3. Equivalent width measurement comparisons for M68-6022 and Car-1087, both observed with the MIKE spectrograph. The three lines represent equal EW values and EW ± ΔEW, where ΔEW = EW_{rms} + 10% EW, and EW_{rms} = 3 mÅ and 6 mÅ, respectively.

For the spectra taken at the VLT with FLAMES/UVES, the higher resolution yields a minimum error of $EW_{rms} = 4$ mÅ, with an exception for Car-1013 where $EW_{rms} = 7$ mÅ due to its lower S/N spectrum.

The reported errors from the DAOSPEC program were lower than those from the revised Cayrel formula, by 1/3 to 1/2. This is due to correlations in the noise estimates in DAOSPEC when the pixel data are rebinned/interpolated during the spectral extractions and wavelength calibrations (P. Stetson 2010, private communication). When individual line measurements were significantly different between the DAOSPEC and *splot* measurements, those lines were checked by eye. These lines tended to be unresolved blends and/or suffered from difficult continuum placement. Since DAOSPEC uses a fixed FWHM and a consistent prescription for continuum placement, those EW measurements were adopted for this analysis, although the ΔEW errors are from the revised Cayrel formula.

A maximum EW of 200 mÅ was adopted for all stars since deviations from the Gaussian profiles used in DAOSPEC become more significant for stronger lines. In fact, for lines $\geqslant$200 mÅ, we found that DAOSPEC would occasionally divide these lines into 2–3 lines, each with lower EWs. The final line lists and measurements were carefully reviewed during this analysis.

3.3. Radial Velocities

Radial velocities were initially measured from five to seven strong lines and refined using DAOSPEC (which cross correlates the measured positions of the detected spectral lines with reference wavelengths from an input line list). Heliocentric corrections were then applied. The radial velocities for the Carina stars are listed in Table 1; the results for the Magellan/MIKE blue and red spectra were averaged together since each arm was reduced independently. The three M68 stars have a mean radial velocity of -95.4 ± 1.0 km s^{-1}, with an average measurement error of 1.5 km s^{-1}. This is in agreement with results in the literature, e.g., Lane et al. (2009) report a radial velocity of -94.93 ± 0.26 km s^{-1} from 123 RGB stars in M68 taken at the 3.9 m Anglo-Australian Telescope with the AAOmega spectrograph. The mean radial velocity of our nine Carina stars is 220.5 ± 4.9 km s^{-1}; the average measurement error of the FLAMES/UVES data is 0.9 km s^{-1}, whereas it is 3.8 km s^{-1} for the metal-poor stars with lower quality Magellan/MIKE spectra. These results are in agreement with the mean radial velocity of 223.9 km s^{-1} found by Koch et al. (2006) for 437 RGB members of Carina, with a dispersion of 7.5 km s^{-1}. The radial velocities from both the high-resolution (this paper) and lower resolution spectra (from Koch et al.) are shown in Table 1; again, these are in good agreement, with a mean difference in $\langle RV_{CaT} - RV_{HR} \rangle = 2.1 \pm 3.4$ km s^{-1}.

3.4. Photometric Parameters (Physical Gravity)

$BVIJK_s$ photometric values for the Carina targets and M68 standard stars are listed in Table 4. *BVI* magnitudes for the M68 stars are from Stetson (2000, on the Johnson-Kron–Cousins scale, Stetson 2005). *J* and K_s magnitudes are from the Two Micron All Sky Survey (2MASS) database.[16] For the Carina members, *VI* magnitudes are from the ESO 2.2 m WFI photometry; initial calibrations were on the default ESO zero-point values, but have been updated to the Johnson-Kron–Cousins scale with Stetson's database and Gullieuszik's photometry (M. Gullieuszik 2009, private communication).

Initial metallicities for the Carina stars are from the CaT measurements (Koch et al. 2006). For the three M68 stars, the average metallicity from Lee et al. (2005) is adopted, [Fe/H] = −2.16.[17]

Color temperatures were found using the Ramírez & Meléndez (2005) calibration and adopted as the initial effective temperatures; see Table 5. Deviations between the different color temperatures are quite small for the three M68 globular cluster stars, i.e., $\sigma_T \leqslant 20$ K from $T(B-V)$, $T(V-I)$, $T(V-J)$, and $T(V-K)$. Deviations are larger for the Carina stars, with $\sigma_T \leqslant 134$ K, and $\langle \sigma_T \rangle = 74$ K. Physical (photometric) gravities are determined using the standard relation

$$\log g = \log g_{\odot} + \log\left(\frac{M_*}{M_{\odot}}\right) + 4 \times \log\left(\frac{T_{\rm eff*}}{T_{\rm eff\odot}}\right) + 0.4 \times (M_{\rm Bol*} - M_{\rm Bol\odot})$$

with $\log g_{\odot} = 4.44$, $T_{\rm eff\odot} = 5777$ K, $M_{\rm Bol\odot} = 4.75$, and adopting a reddening law of $A(V)/E(B-V) = 3.24$. The values of $M_{\rm Bol*}$ are based on the bolometric correction to the *V* magnitude from Alonso et al. (1999), with an assumed distance and stellar mass.

For M68, we adopt the distance and reddening in the Harris (1996) catalog, $(m - M)v = 15.19 \pm 0.10$ and $E(B - V) = 0.05$ from isochrone fitting by McClure et al. (1987). This value

[16] This publication makes use of data products from the Two Micron All Sky Survey which is a joint project of the University of Massachusetts and the Infrared Processing and Analysis Center/California Institute of Technology, funded by the National Aeronautics and Space Administration and the National Science Foundation. The database can be found at http://www.ipac.caltech.edu/2mass/releases/allsky.

[17] Lee et al. (2005) found a mean [Fe II/H] = −2.16 from a high-resolution spectral analysis of eight stars in M68, using photometric gravities. They also find a mean [Fe I/H] = −2.56 using spectroscopic gravities.

Table 4
Target Information

Star	B PBS	V PBS	I PBS	V WFI	I WFI	J 2MASS	K_s 2MASS	B Gul	V Gul	I Gul	J Gul	K Gul
M68-6022	15.127	14.205	13.106	...	...	12.324	11.659	...	...	...	...	...
M68-6023	15.192	14.284	13.191	...	...	12.363	11.712	...	...	...	...	...
M68-6024	15.230	14.354	13.289	...	...	12.479	11.858	...	...	...	...	...
Car-1087	19.146	18.031	16.735	18.00	16.73	15.802	15.301	...	...	...	...	...
Car-5070	19.125	17.904	16.520	17.86	16.49	15.641	14.758	...	...	...	...	...
Car-7002	19.284	18.344	17.146	18.40	17.19	16.244	15.562	...	...	...	...	...
Car-484	19.009	17.603	16.179	17.56	16.16	15.322	14.627	19.055	17.607	16.178	15.290	14.406
Car-524	18.934	17.645	16.308	17.63	16.32	15.388	14.473	18.921	17.598	16.278	15.398	14.574
Car-612	19.077	17.811	16.416	17.82	16.42	15.456	14.763	19.103	17.779	16.403	15.609	14.828
Car-705	19.101	17.828	16.430	17.78	16.43	15.687	14.597	19.104	17.788	16.424	15.509	14.663
Car-769	19.202	18.002	16.693	18.01	16.71	15.698	14.921	19.224	18.025	16.725	15.758	15.040
Car-1013	19.048	17.783	16.424	17.77	16.42	15.515	14.888	19.056	17.767	16.421	15.528	14.726
Car-489	...	...	...	17.85	16.53	15.544	14.933	...	...	...	...	...
Car-837	...	...	...	17.71	16.47	15.456	14.509	19.111	17.705	16.509	15.427	14.621
Car-X	...	...	...	17.51	16.42	15.748	15.223	...	...	...	...	...

Notes. *BVI* from P.B. Stetson's Web site of homogeneous photometry, *VI* from our WFI data, JK_s from the 2MASS database, and *BVIJK* from M. Gullieuszik (2009, private communication).

Table 5
Photometric Parameters

Target	T_{BV} (K)	T_{VI} (K)	T_{VJ} (K)	T_{VK} (K)	$\langle T \rangle$ (K)	σ_T (K)	log g	Mv	Mbol
M68-6022	4663	4671	4677	4694	4676	13	1.53	−0.98	−1.40
M68-6023	4686	4682	4654	4647	4667	20	1.55	−0.91	−1.33
M68-6024	4741	4732	4722	4701	4724	17	1.61	−0.84	−1.23
Car-1087	4391	4457	4572	4416	4459	80	0.95	−2.05	−2.59
Car-5070	4303	4314	4367	4364	4337	33	0.83	−2.19	−2.79
Car-7002	4677	4552	4492	4473	4548	92	1.16	−1.65	−2.15
Car-484	4073	4245	4383	4320	4255	134	0.65	−2.49	−3.14
Car-524	4228	4346	4235	4311	4280	58	0.70	−2.42	−3.05
Car-612	4229	4253	4301	4224	4252	35	0.75	−2.23	−2.88
Car-705	4194	4305	4221	4460	4295	120	0.77	−2.27	−2.89
Car-769	4308	4361	4278	4254	4300	46	0.86	−2.04	−2.65
Car-1013	4208	4280	4372	4250	4278	70	0.75	−2.28	−2.91

Notes. Photometric temperatures are from the Ramírez & Meléndez (2005) calibration. Each temperature is determined from a photometric color, e.g., T_{BV} represents the temperature determined from the $(B - V)$ color. The average of the four color temperatures ($\langle T \rangle$) and standard deviation (σ_T) are listed along with other parameters derived from the magnitudes (see Section 3.4).

is in good agreement with Brocato et al. (1997), but the proper-motion distance modulus, $(m - M)v = 14.91$ (Dinescu et al. 1999) is quite short if this reddening is adopted. A turnoff mass of $0.83 \pm 0.03\,M_\odot$ is found for M68 using isochrones by Vandenberg & Bell (1985).

For Carina, Mighell (1997) determined the distance modulus and reddening from WFPC2 *V*- and *I*-band imaging, but also compares his results in an appendix to the many estimates available in the literature. We adopt Mighell's determination of $(m - M)v = 20.05 \pm 0.11$, which is in excellent agreement with the recent *J* and *K* band photometric determinations by Pietrzyński et al. (2009), and $E(B - V) = 0.06 \pm 0.02$. This reddening value is the same as from the Schlegel et al. (1998) maps. One of the highest values for the distance modulus was found by Monelli et al. (2003; $(m - M)v = 20.24$, with $E(B - V) = 0.03$), but as discussed below (also see Section 5); these differences have negligible effects on our spectral analysis. An estimate of the turnoff mass is more difficult in Carina due to its separate episodes of star formation, each of which has a different turnoff mass; these estimates can have a larger effect on the physical gravity than the distance modulus. Since Carina is dominated by an IA population (5–7 Gyr old), we examined isochrones (Fagotto et al. 1994, with $Y = 0.23$ and $Z = 0.0004$) to find that the age range of 5–12 Gyr corresponds to turnoff masses of 1.0–0.8 $M_\odot$, respectively. We adopted 0.8 $M_\odot$ in this analysis, but note that if 1.0 $M_\odot$ were used, this would change the physical gravities by +0.10 dex with no effect on temperature; this change has only a small effect on the chemical abundances.

3.5. Spectroscopic Parameters

The CaT metallicity and the photometric parameters for temperature and gravity were adopted as the initial stellar parameters for a model atmospheres analysis. Spectroscopic indicators were used to refine the effective temperature and metallicity, as well as to determine the microturbulence values. These values are listed in Table 6. Only the physical gravity is unchanged from the photometric parameters analysis.

3.5.1. Model Atmospheres

The new MARCS spherical models have been adopted in this analysis (Gustafsson et al. 2003, 2008; further expanded by B. Plez 2008, private communications). The grid covers the range of parameters (temperature, luminosity, microturbulence, and metallicity) of RGB stars. The models used in this analysis adopt the Galactic abundance pattern, i.e., $[\alpha/\mathrm{Fe}] = +0.4$ for $[\mathrm{Fe/H}] \leqslant -1.0$, which is the metallicity range of the stars in Carina. We adopt the standard version of the MOOG[18] (Sneden 1973) spectral synthesis code to determine the individual line abundances. Corrections were applied when necessary for continuum scattering effects that can affect the results for lines below 5000 Å, as described in Section 3.8.2. The photometric gravities were retained throughout the analysis (see Section 3.8.3).

3.5.2. Effective Temperatures, Microturbulence, and Metallicity

The effective temperatures were refined from the photometric values through examination of the Fe I lines. Only lines redward 5000 Å were considered to avoid uncertainties in the

[18] The 2009 version of MOOG is available from http://www.as.utexas.edu/~chris/moog.html.

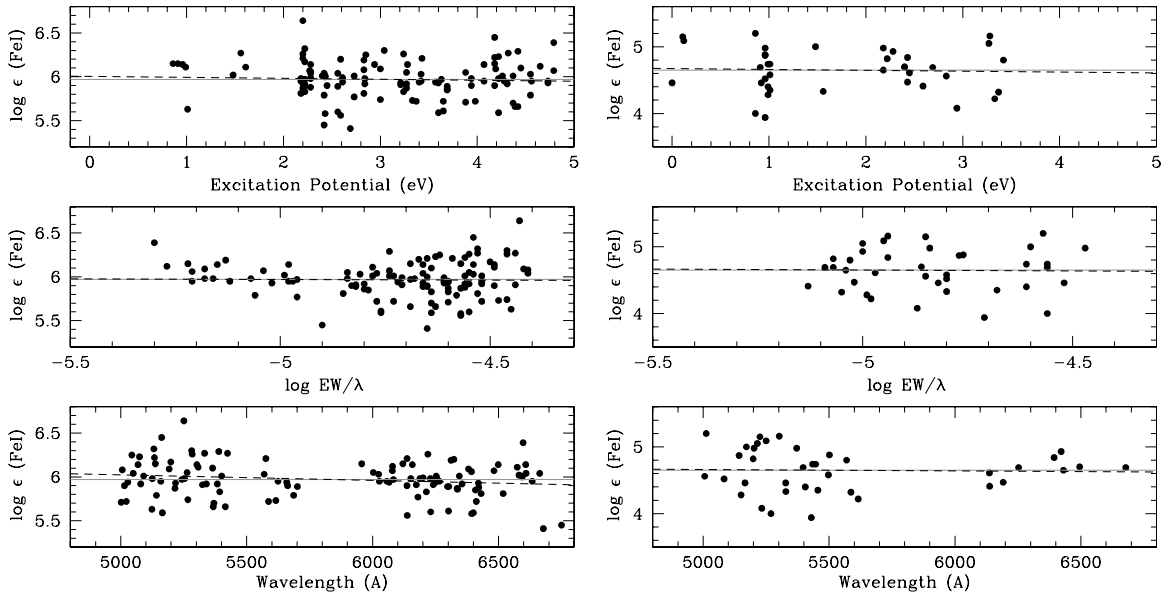

Figure 4. MOOG results for Car-484 (left panel), a moderate S/N high-resolution FLAMES/UVES spectrum, and Car-7002, a moderate S/N and moderate resolution Magellan/MIKE spectrum. These plots show that the Fe I line abundances are minimized with excitation potential (to determine surface temperature), equivalent width (to define microturbulence), and wavelength (a check on the sky subtraction).

Table 6
Spectroscopic Parameters (Photometric Gravities)

Target	$T_{\rm eff}$ (K)	log g_* (cgs)	ξ (km s^{-1})	12+log(Fe I) $\pm\delta$(Fe)[a]	[Fe I/H] $\pm\sigma$ (#)	CaT (S10)[b]
M68-6022	4550 ± 44	1.53 ± 0.04	1.50 ± 0.12	4.99 ± 0.02	−2.51 ± 0.23 (92)	−2.16
M68-6023	4667 ± 55	1.55 ± 0.04	1.60 ± 0.12	5.09 ± 0.03	−2.41 ± 0.24 (92)	−2.16
M68-6024	4650 ± 56	1.61 ± 0.04	1.80 ± 0.12	4.86 ± 0.03	−2.64 ± 0.24 (81)	−2.16
Car-1087	4600 ± 98	0.95 ± 0.10	2.45 ± 0.25	4.69 ± 0.06	−2.81 ± 0.34 (38)	−3.10
Car-5070	4550 ± 81	0.83 ± 0.10	2.30 ± 0.20	5.35 ± 0.05	−2.15 ± 0.38 (55)	−2.57
Car-7002	4548 ± 96	1.16 ± 0.10	2.00 ± 0.24	4.64 ± 0.05	−2.86 ± 0.33 (38)	−3.29
Car-484	4400 ± 66	0.65 ± 0.10	2.30 ± 0.07	5.97 ± 0.02	−1.53 ± 0.21 (114)	−1.62
Car-524	4500 ± 64	0.70 ± 0.10	2.40 ± 0.07	5.75 ± 0.02	−1.75 ± 0.21 (121)	−1.61
Car-612	4500 ± 61	0.75 ± 0.10	2.10 ± 0.08	6.20 ± 0.02	−1.30 ± 0.23 (126)	−1.84
Car-705	4500 ± 61	0.77 ± 0.10	2.10 ± 0.07	6.15 ± 0.02	−1.35 ± 0.25 (127)	−1.63
Car-769	4600 ± 76	0.86 ± 0.10	2.30 ± 0.08	5.82 ± 0.02	−1.68 ± 0.25 (125)	−1.63
Car-1013	4600 ± 105	0.75 ± 0.10	2.20 ± 0.11	6.20 ± 0.03	−1.30 ± 0.37 (125)	−1.58

Notes.
[a] δ(Fe) is the error in the mean of the Fe I lines (see Section 4.2).
[b] CaT metallicities from the calibration by Starkenburg et al. (2010). For the three M68 stars, CaT metallicities are from Lee et al. (2005).

standard MOOG treatment of scattering in the continuous opacity (see Section 3.8.2). Microturbulence values were found by minimizing the slope in the Fe I line abundances with EW. Similarly, the excitation temperatures were found by minimizing the slope in the same Fe I line abundances with excitation potential (χ, in eV). While the M68 stars had lower excitation than color temperatures (by an average of 67 K), the Carina stars had higher excitation temperatures (by an average of 200 K). The final metallicity (for which we adopt the [Fe I/H] values) is also found at the end of these minimization iterations.

No significant relationship was found in the Fe I abundances versus wavelength (>5000 Å) for either the globular cluster or the Carina targets; this indicates that the sky subtraction and overall data reduction methods were successful. Eliminating lines with $\chi < 1.4$ eV, which can be particularly sensitive to departures from local thermodynamic equilibrium (LTE) effects, also had no significant effect on the temperature or microturbulence values. Samples of these relationships are shown in Figure 4 for two stars, one observed with the FLAMES/UVES spectrograph and the other observed with the MIKE spectrograph. Adjusting the metallicities from the initial CaT values had no significant effect on the excitation temperatures ($\Delta T < 10$ K). Adopting the spectroscopic temperatures had only a small effect on the photometric gravities ($\leqslant$+0.08 in the Carina stars and $\leqslant -0.02$ for the M68 stars).

Four stars in Carina have been observed and analyzed independently by Koch et al. (2008a). Their analysis with ATLAS9 models atmospheres results in excitation temperatures that are in excellent agreement with ours, with differences ranging from $\Delta T = +116$ to -70 K, and with an average offset of +32 K. The differences in microturbulence are more significant, with Koch et al.'s values being $\sim$0.50 km s^{-1} lower. This is linked to differences in our gravity determinations discussed in Section 3.8.3.

3.6. Stellar Parameter Error Estimates

Stellar parameters and their uncertainties are listed in Table 6. The 1σ uncertainty in the effective temperature is determined from the slope in the Fe I line abundances versus excitation potential (χ) allowing the change in the iron abundance to equal the standard deviation σ(Fe I). Similarly, the 1σ uncertainty in microturbulence is determined by setting the slope of the Fe I line abundances versus EW equal to σ(Fe I).

For the physical gravities, the uncertainties are determined from errors in the distance moduli, reddening, and stellar mass (see Section 3.4). For M68, the uncertainty in the turnoff mass is tiny ($\pm 0.03\ M_{\odot}$), which has a negligible effect on the gravity ($\Delta \log\ g = \pm 0.04$). The uncertainties in gravity are also very small when the short distance modulus reported by Dinescu et al. (1999) is adopted for M68 ($\Delta \log\ g = \pm 0.07$). For Carina, the dominant uncertainty is from the stellar mass. The range in turnoff masses for Carina is 0.8–1.0 $M_{\odot}$ due to its episodic star formation history; the resulting uncertainties in log g can be as large as 0.10 dex.

Uncertainties in metallicity are adopted from the error in the mean of the Fe I abundances (see Section 4.2).

3.7. Spectrum Syntheses and Hyperfine Structure Corrections

Spectrum syntheses were carried out for Na I (5688, 5889, 5895), Mg I (3829, 3832), Sr II (4077, 4205), Ba II (4554, 5853, 6141, 6496), and Eu II (4129, 4205, 6645). In each case, the instrumental resolution of the spectrum was adopted as the main source of broadening, and checked with the shapes and EW abundance results from nearby spectral lines (Fe, Ca, and Ti). When an EW could be measured, the synthetic and EW abundance results were compared; when excellent agreement was found then the EW result was taken. Line abundances taken from the synthetic results are noted in Tables 2 and 3.

Hyperfine structure (HFS) corrections were determined from spectrum syntheses for the odd-Z elements (Sc II, V I, Mn I, and Co I), Cu I, and the neutron-capture elements Ba II, La II, and Eu II. HFS components were taken from Lawler et al. (2001a; La II), Booth et al. (1983; Mn I), Prochaska et al. (2001; Sc II, V I, Mn I, and Co I), and the Kurucz database[19] for the remaining lines. HFS components and isotopic ratios for Cu I are from Biehl (1976), for Eu II from Lawler et al. (2001b), and for Ba II from McWilliam (1998; r-process isotopic ratios were adopted for the most metal-poor stars, whereas the solar ratios were used for stars with [Fe/H] > -2).

3.8. Other Considerations

3.8.1. Spherical versus Plane Parallel

Spherical MARCS models represent a significant improvement in the modeling of stellar atmospheres, e.g., Heiter & Eriksson (2006) recommend the use of spherical model atmospheres in abundance analyses for stars with log $g < 2$ and $4000\ \mathrm{K} \leqslant T_{\rm eff} \leqslant 6500\ \mathrm{K}$, which encompasses the range in stellar parameters of our target stars. Tests performed by Tafelmeyer et al. (2010) showed systematic offsets between the spherical and plane-parallel models are below 0.15 dex (this includes iron lines and other elements, e.g., [C/Fe]).

We performed similar tests, comparing the metallicities we determined from spherical MARCS models to those from plane-parallel MARCS (pp-MARCS) and Kurucz models. The pp-MARCS models had the effect of reducing the excitation temperature results by $\sim$100 K, but the Kurucz models had a different effect, increasing the microturbulence values by $\sim$0.1 km s^{-1}. In both cases, all other parameters were unchanged. These offsets, when applied to the abundance analysis, changed the Fe I abundances by only $\sim$0.05 dex (+0.05 with pp-MARCS models and -0.05 with Kurucz models). This is very similar to the offsets found by Tafelmeyer et al. (2010) and Heiter & Eriksson (2006) for iron.

[19] http://kurucz.harvard.edu/LINELISTS/GFHYPERALL

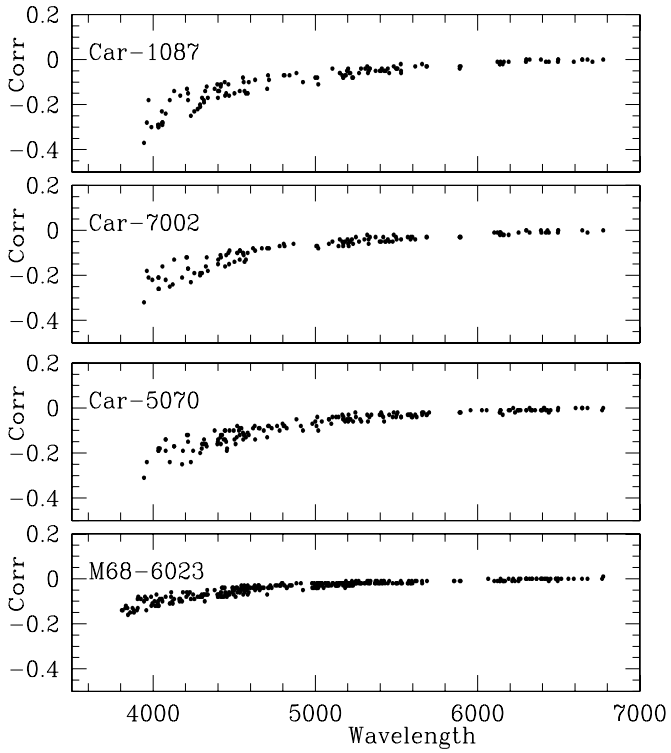

Figure 5. Comparison of the line abundance *corrections* from MOOG-SCAT for one of the M68 standard star and the three most metal-poor stars in Carina. The y-label "Corr" = MOOG-SCAT − MOOG.

3.8.2. Continuum Scattering Effects

The standard version of MOOG treats continuum scattering (σ_{ν}) as if it were absorption (κ_{ν}) in the source function, i.e., $S_{\nu} = B_{\nu}$ (the Planck function), an approximation that is only valid at long wavelengths in RGB stars. At shorter wavelengths ($\leqslant$5000 Å), Cayrel et al. (2004) have shown that the scattering term must be taken into account such that the source function becomes $S_{\nu} = (\kappa_{\nu}\ B_{\nu} + \sigma_{\nu}\ J_{\nu})/(\kappa_{\nu} + \sigma_{\nu})$. A new version of MOOG (MOOG-SCAT; Sobeck et al. 2010) has been used to test our results and calculate corrections to our abundances line by line. As shown in Figure 5, the scattering corrections are negligible for red lines, but can approach 0.4 dex in the blue. Lines with the largest corrections are the resonance lines of Mn I. Note also that the corrections are sensitive to the atmospheric parameters, in particular metallicity; the three stars in Carina that are shown were choosen because they have the largest corrections and they are the most metal poor.

We compared the elemental abundances between the programs MOOG and CALRAI (Spite 1967; Cayrel et al. 1991; V. Hill et al. 2012, in preparation), and also the scattering corrections calculated with MOOG-SCAT to those determined with the program Turbospectrum (Alvarez & Plez 1998); the standard abundance results and scattering corrections were nearly identical for all lines between these codes; in particular, the

scattering corrections were in agreement to within ∼0.01 dex. Only the resonance lines of Mn I showed slightly larger differences in the scattering corrections (∼0.04 dex); since resonance lines form over more atmospheric layers, we expect that these lines are more sensitive to the details in the models and the line formation calculations between the codes. Thus, we consider the consistency in the abundance results from the line formation codes MOOG and CALRAI, and the scattering corrections between MOOG-SCAT and Turbospectrum to be in excellent agreement.

As a final note, the scattering corrections had no effect on our spectroscopic temperature or microturbulence determinations, nor the metallicities for [Fe I/H], since only Fe I lines with $\lambda > 5000$ Å were used in those steps.

3.8.3. Gravity is Not from Fe I/Fe II

The analysis of ten stars in Carina by Koch et al. (2008a) and five more stars by Shetrone et al. (2003) used the Fe II lines to determine spectroscopic gravities from ionization equilibrium (where [Fe I/H] = [Fe II/H]). For four stars in common with Koch et al., our gravities are smaller than theirs by $\log g \sim 0.5$ dex. Since turbulent velocity and ionization equilibrium are correlated in RGBs, then the higher microturbulent values found by Koch et al. (see Section 3.5.2) are correlated with their higher spectroscopic gravities.

There are sufficient Fe II lines in many of the stars in our analysis to examine the ionization equilibrium of iron and determine spectroscopic gravities, however we do not use this method in this analysis. For consistency with the FLAMES/GIRAFFE analysis, where a shorter wavelength interval meant fewer Fe II lines, then we adopt photometric gravities using the same methods as in Lemasle et al. (2012). On the other hand, we note that the Fe I and Fe II abundances are in good agreement for our Carina targets, with a mean [Fe II/Fe I] = +0.02, and range of −0.24 to +0.20, which is $\sim 1\sigma$(Fe I). The stars in M68 have higher offsets, with a mean [Fe II/Fe I] = +0.35, which may reflect uncertainties in its distance or reddening. When the abundance of Fe II is found to be larger than Fe I in red giants, it can be due to the overionization of Fe I by the radiation field, which is neglected under the assumption of LTE. Corrections for this effect can be as large as 0.3 dex (Mashonkina et al. 2010), which is similar to the offset in the M68 stars. Thus, we consider our Fe I and Fe II results to be in good agreement for all of our targets when physical gravities are adopted.

Note, Fe II lines at all wavelengths were examined in this analysis, i.e., they were not restricted to $\lambda < 5000$ Å like Fe I.

3.9. Evaluating the CaT Metallicity

The initial metallicities in our analysis are taken from a calibration of the near-IR Ca II triplet near 8500 Å(=CaT). A direct comparison between the low-resolution CaT metallicity index and high-resolution iron abundances for large samples of RGB stars in the dwarf galaxies Fornax and Sculptor was shown by Battaglia et al. (2008) to provide consistent abundances in the range $-2.5 <$ [Fe/H] < -0.5. More recently, Starkenburg et al. (2010) found that the metallicities deviate strongly from the linear relationship for RGB stars with [Fe/H] < -2.0 and have developed a new calibration for metal-poor stars that also considers the [Ca/Fe] ratio.

The CaT metallicities for our targets are listed in Table 6 and plotted against the [Fe I/H] values in Figure 6. The high-resolution [Fe I/H] abundances tend to be slightly larger than the metallicities from the CaT index, however, as Starkenburg et al. (2010) show, the ratio of [Ca/Fe] becomes more important in the calibration of low-metallicity stars. The two most metal-poor stars in this analysis are found to have lower [Ca/Fe] ratios than the Galactic trend that was assumed in the Starkenburg et al. calibration.

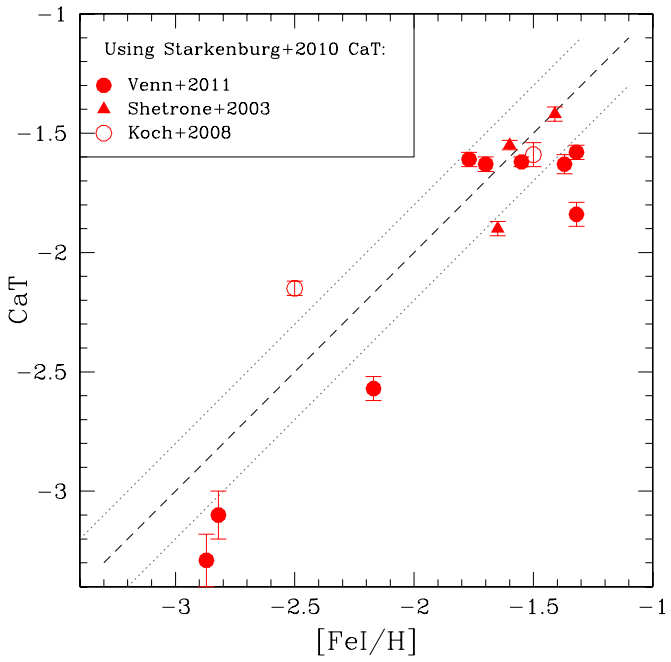

Figure 6. Iron abundances ([Fe I/H]) from high-resolution spectral analyses vs. those derived from the CaT calibration by Starkenburg et al. (2010). A line of equal metallicities is shown (dashed), ±0.2 dex (dotted).

(A color version of this figure is available in the online journal.)

4. ABUNDANCE RESULTS

4.1. Solar Abundances and Galactic Comparisons

For comparison purposes, solar abundances from Asplund et al. (2009) are adopted. Galactic comparisons are from the compilation by Venn et al. (2004), supplemented with Si, V, Cr, and Nd from Fulbright (2000). The compilation was updated with thick disk stars from Reddy et al. (2006), La from the compilation by Roederer et al. (2010), and Cu and Zn from Mishenina et al. (2002). All of these were rescaled to Asplund et al. (2009) solar abundances from the Grevesse & Sauval (1998) values. The compilation of abundances of metal-poor stars in the Galactic halo and Local Group dwarf galaxies by Frebel (2010; after eliminating the upper limit values) was also used here for comparison purposes. Previously published abundances for Carina and M68 were rescaled to the Asplund et al. (2009) solar abundances, i.e., Shetrone et al. (2003) and Lee et al. (2005) from Grevesse & Sauval (1998), and Koch et al. (2008a) from Asplund et al. (2005) values.

4.2. Abundance Error Estimates

Errors in the abundances have been determined in two ways, with the maximum of these errors adopted for the analysis (Tables 7–9). First, the error in the EW measurements are conservatively estimated as $\Delta EW = EW_{rms} + 10\% \times EW$, where EW_{rms} is from the Cayrel formula (Section 3.2). This ΔEW was propagated through the abundance analysis to provide a σ(EW) in each line abundance. This error is not necessarily symmetric,

Table 7
Abundance Uncertainties for M68-6023

Elements	$\Delta T_{\rm eff}$ +55	$\Delta\log g$ −0.04	$\Delta\xi$ +0.12	Δ[Fe/H] −0.02	Added in Quadrature
Fe I	+0.09	0.00	−0.05	0.01	0.10
Fe II	−0.02	−0.02	−0.05	−0.01	0.06
CH	+0.05	−0.04	0.00	0.00	0.06
Na I	+0.08	+0.01	−0.03	0.01	0.09
Mg I	+0.08	+0.02	−0.03	0.01	0.09
Ca I	+0.08	+0.01	−0.04	0.01	0.09
Sc II	+0.02	−0.01	−0.05	−0.01	0.06
Ti I	+0.09	+0.01	−0.04	0.01	0.10
Ti II	+0.02	−0.01	−0.05	−0.01	0.06
V I	+0.06	0.00	−0.03	0.01	0.07
Cr I	+0.10	+0.01	−0.05	0.01	0.11
Mn I	+0.10	0.00	−0.07	0.01	0.12
Co I	+0.10	+0.01	−0.08	0.01	0.13
Ni I	+0.09	+0.01	−0.05	0.01	0.11
Zn I	+0.01	0.00	−0.02	0.00	0.02
Sr II	+0.04	−0.01	−0.08	0.01	0.09
Y II	+0.02	−0.01	−0.03	−0.01	0.04
Zr II	+0.02	−0.02	−0.02	−0.01	0.03
Ba II	+0.04	−0.02	−0.09	−0.01	0.10
Eu II	+0.03	−0.02	−0.09	−0.01	0.10

Table 8
Abundance Uncertainties for CAR-1087

Elements	$\Delta T_{\rm eff}$ +98	$\Delta\log g$ −0.10	$\Delta\xi$ −0.25	Δ[Fe/H] −0.06	Added in Quadrature
Fe I	+0.10	0.00	+0.08	+0.01	0.13
Fe II	−0.03	−0.02	+0.08	−0.01	0.09
Na I	+0.13	0.00	+0.06	+0.01	0.15
Mg I	+0.05	+0.02	+0.04	+0.01	0.07
Ca I	+0.08	+0.01	+0.02	+0.01	0.09
Sc II	+0.03	−0.02	+0.06	−0.01	0.07
Ti I	+0.17	+0.01	+0.08	+0.01	0.19
Ti II	0.00	−0.02	+0.08	−0.01	0.08
V I	+0.13	+0.02	+0.04	+0.01	0.14
Cr I	+0.18	+0.01	+0.09	+0.02	0.20
Mn I	+0.18	+0.02	+0.10	+0.02	0.21
Ni I	+0.07	+0.01	+0.03	+0.01	0.08
Ba II	+0.08	−0.04	+0.02	−0.01	0.09
Eu II	+0.04	−0.03	+0.02	−0.01	0.06

and we adopt the average. For synthetic spectra, σ(EW) was estimated from the range of abundances for which a good fit of the observed line profile could be achieved. The second method for estimating the error in the abundances is simply to calculate the standard deviation when more than five lines of an element are available, $\sigma(X)$; when fewer lines are available, we set $\sigma(X) = \sigma$(Fe I). The final error in [X/H] is adopted as the maximum of $\sigma(X)$ or σ(EW). The corresponding error on the mean, $\delta(X)$, is calculated as

$$\delta(X) = \sigma(X)/\sqrt{N_X},$$

where N_X is the number of lines available of element X. To get the final error in [X/Fe], i.e., the ratio with iron, then the error on the mean (δ(Fe I)) was added in quadrature.

These line measurement errors do not take into account the errors due to the uncertainties in the stellar parameters. These errors are difficult to ascertain and combine properly since they are not independent and their relationship(s) to one another are not well defined. We report these errors for three representative stars, Car-6023, Car-1087, and Car-484, in Tables 7–9. These three stars represent the range in stellar parameters, resolution, and S/N of all of our spectra. It can be seen that the stellar parameter errors are similar to or smaller than the line measurement errors (exceptions include Ca I, Ti I, Cr I, and Co I where the stellar parameter errors can be slightly larger, but still $\leqslant$0.15 dex).

Table 9
Abundance Uncertainties for Car-484

Elements	$\Delta T_{\rm eff}$ +66	$\Delta\log g$ −0.1	$\Delta\xi$ +0.07	Δ[Fe/H] −0.02	Added in Quadrature
Fe I	+0.06	−0.01	−0.04	0.00	0.07
Fe II	−0.07	−0.05	−0.03	0.00	0.09
O I	0.00	−0.05	−0.01	−0.01	0.05
Na I	+0.06	+0.01	−0.01	0.00	0.06
Mg I	+0.05	+0.01	−0.03	0.00	0.06
Si I[a]	0.00	−0.01	0.00	−0.01	0.01
Ca I	+0.09	+0.01	−0.03	0.00	0.10
Sc II	−0.02	−0.03	−0.02	0.00	0.04
Ti I	+0.13	−0.01	−0.04	0.00	0.14
Ti II	−0.03	−0.05	−0.04	0.00	0.07
V I	+0.14	−0.01	−0.01	0.00	0.14
Cr I	+0.14	−0.01	−0.05	0.00	0.15
Mn I	+0.10	0.00	−0.03	0.00	0.11
Co I	+0.08	−0.02	−0.03	0.00	0.08
Ni I	+0.04	−0.01	−0.03	0.00	0.05
Cu I	+0.08	−0.02	−0.04	0.00	0.08
Zn I	−0.04	−0.02	−0.03	0.00	0.05
Y II	0.00	−0.04	−0.03	0.00	0.05
Ba II	+0.01	−0.06	−0.06	0.00	0.08
La II	+0.01	−0.06	−0.01	−0.01	0.06
Nd II	0.00	−0.05	−0.03	0.00	0.06
Eu II	−0.01	−0.05	−0.01	−0.01	0.05

Note. [a] Si I errors determined from the lines and EWs in Car-524.

Car-1087 can be applied to Car-5070 and Car-7002. Those for Car-484 can be applied to the rest of the FLAMES/UVES sample, although the lower S/N for Car-1013 means the errors for that target are larger by $\sim$2$\times$ (as seen in Table 6).

4.3. M68 Comparison Stars

The three stars analyzed here in M68 are $\sim$1.4 magnitudes fainter than one M68 star analyzed by Shetrone et al. (2003) and eight stars analyzed by Lee et al. (2005); thus they are located further down the RGB and have slightly higher temperatures and gravities. Our microturbulence values are comparable or lower.

Chemical abundances determined here for three stars in M68 are listed in Table 10. The metallicities from Fe I are in excellent agreement with one another, as expected for a single stellar population. The mean Fe I abundance is log(Fe I/H) = 5.04 $\pm$ 0.10, where the error is the line to line abundance scatter in each star, added in quadrature, and divided by $\sqrt{3}$. This is similar to the mean [Fe I/H] abundance determined by Lee et al. (2005), where [Fe I/H] = 4.96 $\pm$ 0.06 when they adopt the photometric gravities. Higher iron abundances are found with lower spectroscopic gravities; this is also seen by Shetrone et al. (2003) for one star.

Most of the elemental abundances determined here are in excellent agreement with those from Lee et al. (2005) and Shetrone et al. (2003), and our Na I values are within the ranges of the others. To compare the [X/Fe] *ratios* for these elements

Table 10
M68 Chemical Abundances

Elements	6022 [X/Fe] ±σ (#)	6023 [X/Fe] ±σ (#)	6024 [X/Fe] ±σ (#)
Fe I	4.99 ± 0.02 (92)	5.09 ± 0.03 (92)	4.86 ± 0.03 (81)
Fe II	0.40 ± 0.05 (19)	0.26 ± 0.05 (19)	0.39 ± 0.06 (17)
CH	−0.82 ± 0.20 (S)	−0.62 ± 0.20 (S)	−0.59 ± 0.20 (S)
O I	<1.36	<1.33	<1.54
Na I[a]	0.07 ± 0.10 (S)	0.27 ± 0.10 (S)	−0.03 ± 0.10 (S)
Mg I	0.01 ± 0.20 (S)	−0.09 ± 0.20 (S)	0.04 ± 0.20 (S)
Si I	<1.22	<1.15	<1.36
Ca I	0.48 ± 0.04 (17)	0.39 ± 0.04 (16)	0.48 ± 0.05 (15)
Sc II	0.57 ± 0.05 (10)	0.28 ± 0.10 (10)	0.44 ± 0.06 (9)
Ti I	0.11 ± 0.05 (23)	0.12 ± 0.04 (21)	0.30 ± 0.07 (20)
Ti II	0.77 ± 0.05 (52)	0.54 ± 0.05 (51)	0.65 ± 0.05 (46)
V I	−0.06 ± 0.16 (2)	0.02 ± 0.17 (2)	0.35 ± 0.17 (2)
Cr I	−0.17 ± 0.06 (12)	−0.25 ± 0.09 (12)	−0.17 ± 0.08 (9)
Mn I[a]	−0.48 ± 0.07 (7)	−0.61 ± 0.12 (7)	−0.31 ± 0.10 (4)
Co I	−0.27 ± 0.09 (6)	−0.26 ± 0.06 (7)	0.10 ± 0.10 (6)
Ni I	0.06 ± 0.03 (8)	0.20 ± 0.10 (8)	0.04 ± 0.14 (7)
Zn I	0.47 ± 0.16 (2)	0.33 ± 0.17 (2)	0.43 ± 0.24 (1)
Sr II	−0.08 ± 0.16 (2)	−0.26 ± 0.17 (2)	−0.23 ± 0.17 (2)
Y II	−0.07 ± 0.23 (1)	−0.43 ± 0.17 (2)	−0.21 ± 0.17 (2)
Zr II	0.20 ± 0.23 (1)	−0.05 ± 0.24 (1)	0.00 ± 0.24 (1)
Ba II	0.33 ± 0.12 (4)	0.14 ± 0.12 (4)	0.36 ± 0.12 (4)
La II	<1.37	<1.36	<1.56
Nd II	···	···	1.27 ± 0.24 (1)
Eu II	···	0.24 ± 0.17 (2)	0.47 ± 0.17 (2)

Notes. We calculate [X/Fe] = [X/H] − [Fe I/H]. For Fe I, the abundance listed is 12 + log(Fe/H).
[a] A correction of Δ[Na/Fe] = −0.5 has been applied to account for NLTE effects on the Na D lines (Andrievsky et al. 2007). Similarly, we apply a correction of Δlog (Mn/H) = +0.5 to the Mn I resonance lines to account for NLTE effects (Bergemann & Gehren 2008).

Table 11
Carina Chemical Abundances

Elements	484 [X/Fe] ±σ (#)	524 [X/Fe] ±σ (#)	612 [X/Fe] ±σ (#)
Fe I	5.97 ± 0.02 (114)	5.75 ± 0.02 (121)	6.20 ± 0.02 (126)
Fe II	0.07 ± 0.04 (14)	0.09 ± 0.03 (15)	0.12 ± 0.05 (18)
O I	0.40 ± 0.21 (1)	0.41 ± 0.21 (1)	<0.09
Na I	−0.25 ± 0.21 (1)	< −0.26	< −0.72
Mg I	0.19 ± 0.15 (2)	0.27 ± 0.15 (2)	−0.50 ± 0.16 (2)
Si I	···	0.60 ± 0.15 (2)	0.13 ± 0.23 (1)
Ca I	0.16 ± 0.04 (20)	0.10 ± 0.04 (19)	−0.17 ± 0.04 (19)
Sc II	0.06 ± 0.04 (12)	−0.08 ± 0.04 (10)	−0.74 ± 0.07 (8)
Ti I	0.23 ± 0.04 (25)	−0.02 ± 0.03 (22)	−0.42 ± 0.04 (18)
Ti II	0.18 ± 0.05 (13)	0.03 ± 0.06 (13)	−0.29 ± 0.05 (12)
V I	0.01 ± 0.03 (10)	0.21 ± 0.15 (2)	−0.67 ± 0.23 (1)
Cr I	0.00 ± 0.12 (4)	−0.09 ± 0.10 (4)	−0.20 ± 0.12 (4)
Mn I	−0.27 ± 0.05 (7)	−0.34 ± 0.10 (4)	−0.51 ± 0.10 (6)
Co I	−0.13 ± 0.21 (1)	−0.27 ± 0.21 (1)	< −0.86
Ni I	−0.07 ± 0.04 (15)	−0.08 ± 0.04 (14)	−0.46 ± 0.04 (14)
Cu I	−0.47 ± 0.21 (1)	< −0.85	< −1.60
Zn I	0.16 ± 0.21 (1)	−0.17 ± 0.21 (1)	−0.83 ± 0.23 (1)
Y II	−0.32 ± 0.12 (3)	−0.46 ± 0.12 (3)	−1.37 ± 0.16 (2)
Ba II	0.16 ± 0.26 (1)	0.09 ± 0.21 (1)	−0.64 ± 0.16 (S)
La II	0.48 ± 0.12 (3)	0.55 ± 0.15 (2)	<0.11
Nd II	0.63 ± 0.15 (2)	0.52 ± 0.15 (2)	−0.56 ± 0.23 (1)
Eu II	0.47 ± 0.21 (1)	<0.63	<0.26

Notes. We calculate [X/Fe] = [X/H] − [Fe I/H]. For Fe I, the abundance listed is 12 + log(Fe/H).

with those from Lee et al. requires knowing that their [X/Fe] results use Fe I for ratios with neutral species and Fe II for ratios with ionized species and oxygen. In our analysis, we use only the Fe I lines to indicate the metallicity, thus we adjust their [X/Fe II] abundances by adding their [Fe II/Fe I] ratio, = +0.40.

The most significant differences are that our Mg and Mn abundances are lower than Lee et al.'s (2005), and the Shetrone et al.'s (2003) values for Zn, Y, Ba, and Eu are lower (see figures in the next sections). For the heavy elements examined by Shetrone et al., we track the differences to the model atmosphere parameters, e.g., ionized species that are more sensitive to gravity, and Zn abundances that are ∼2× more sensitive to temperature than the other elements. For Mn, we note that Lee et al. examined only a single, very weak line (Mn I 6021.8), whereas ours are from several lines that are in good agreement with one another, thus we consider our result more reliable. For Mg, our abundances have been determined from four spectral lines—three lines from spectrum synthesis due to severe blending and difficulties in the continuum placements (two near 3830 Å and one at λ5172), and a fourth line at λ5528, which is sufficiently unblended to be analyzed from EW measurements (note that a fifth line is available in the FLAMES/UVES spectra at λ5711 but is too weak to be measured in any of the Magellan/MIKE spectra). The Mg abundances are consistent between these four lines and from star to star in M68, however we assign a larger uncertainty to account for the difficulties in setting the continuum in the three line syntheses. The average [Mg/Fe] is slightly lower than that found in the other analyses (Lee et al. 2005; Shetrone et al. 2003), than the Galactic trends at that metallicity, and than what is found in the other α-elements. While the offset is within the estimated uncertainties, we note that our [Na/Fe] are slightly higher than the Galactic trends—it is possible these stars exhibit some deep mixing (e.g., Gratton et al. 2010).

New elemental abundances not previously determined in M68 (Sr II and Zr II) are in good agreement with the Galactic distributions. Finally, our upper limits for Si I, O I, and La II are in agreement with the abundances determined by Lee et al. (2005) and Shetrone et al. (2003).

Thus, our M68 results appear to be in good agreement with other abundance determinations for this cluster, and Galactic cluster and field stars in general. We conclude that our stellar parameter determinations and model atmospheres analyses can therefore be used reliably for elemental abundances in the Carina targets.

4.4. Carina Stars

The chemical abundances of the stars in Carina are presented in Tables 11–13 and discussed element by element in the following sections.

4.4.1. Carbon

Carbon forms during the helium burning phases, whether the hydrostatic helium core burning phases in massive stars, or helium shell burning phases in asymptotic giant branch (AGB) stars (Woosley & Weaver 1995). The chemical evolution of carbon is further complicated by CNO cycling, where carbon is reduced when exposed to hot protons and the CN cycle runs to equilibrium values. This evolution in carbon can be seen in RGB stars in globular clusters, where the [C/H] abundance and $^{12}C/^{13}C$ ratio are both reduced as stars ascend the RGB due to internal (self) mixing (Gratton et al. 2004).

Carbon abundances in this analysis were determined from spectrum syntheses of portions of the $A^2\Pi$ - $X^2\Delta$ CH G band near λ4320 in the Magellan spectra. The best fit was taken as the

Table 12
Carina Chemical Abundances Continued

Elements	705 [X/Fe] ±σ (#)	769 [X/Fe] ±σ (#)	1013 [X/Fe] ±σ (#)
Fe I	6.15 ± 0.02 (127)	5.82 ± 0.02 (125)	6.20 ± 0.03 (125)
Fe II	0.02 ± 0.06 (16)	0.06 ± 0.05 (15)	−0.24 ± 0.06 (17)
O I	<0.12	···	<0.08
Na I	−0.22 ± 0.25 (1)	0.04 ± 0.25 (1)	−0.25 ± 0.37 (1)
Mg I	0.13 ± 0.18 (2)	0.42 ± 0.18 (2)	0.09 ± 0.26 (2)
Si I	0.23 ± 0.25 (1)	0.45 ± 0.18 (2)	0.06 ± 0.26 (2)
Ca I	0.11 ± 0.04 (19)	0.24 ± 0.06 (21)	−0.06 ± 0.05 (20)
Sc II	−0.03 ± 0.05 (11)	0.15 ± 0.06 (11)	−0.24 ± 0.07 (13)
Ti I	0.02 ± 0.05 (25)	0.27 ± 0.05 (23)	0.27 ± 0.06 (24)
Ti II	−0.01 ± 0.06 (11)	0.13 ± 0.06 (11)	0.11 ± 0.09 (13)
V I	0.02 ± 0.06 (10)	0.41 ± 0.11 (5)	0.09 ± 0.08 (11)
Cr I	−0.23 ± 0.12 (4)	0.08 ± 0.12 (4)	0.25 ± 0.21 (3)
Mn I	−0.30 ± 0.07 (7)	0.02 ± 0.11 (5)	−0.51 ± 0.17 (5)
Co I	−0.26 ± 0.25 (1)	0.02 ± 0.25 (1)	−0.01 ± 0.26 (2)
Ni I	−0.04 ± 0.04 (17)	0.03 ± 0.04 (13)	−0.10 ± 0.06 (17)
Cu I	−0.80 ± 0.25 (1)	−0.55 ± 0.25 (1)	···
Zn I	−0.05 ± 0.25 (1)	···	−0.46 ± 0.37 (1)
Y II	−0.63 ± 0.18 (2)	−0.27 ± 0.14 (3)	−0.32 ± 0.21 (3)
Ba II	−0.61 ± 0.14 (3)	−0.17 ± 0.14 (3)	−0.15 ± 0.26 (S)
La II	<0.15	···	<0.14
Nd II	0.26 ± 0.18 (2)	0.27 ± 0.18 (2)	0.11 ± 0.26 (2)
Eu II	<0.31	<0.63	0.33 ± 0.37 (1)

Notes. We calculate [X/Fe] = [X/H] − [Fe I/H]. For Fe I, the abundance listed is 12 + log(Fe/H).

Table 13
Carina Chemical Abundances

Elements	1087 [X/Fe] ±σ (#)	5070 [X/Fe] ±σ (#)	7002 [X/Fe] ±σ (#)
Fe I	4.69 ± 0.06 (38)	5.35 ± 0.05 (55)	4.64 ± 0.05 (38)
Fe II	0.01 ± 0.07 (7)	−0.14 ± 0.10 (11)	0.20 ± 0.14 (6)
CH	< −1.02 (S)	< −0.98 (S)	< −1.07 (S)
O I	<1.55	<0.90	<1.61
Na I[a]	−0.82 ± 0.24 (S)	−1.18 ± 0.38 (S)	−0.45 ± 0.23 (S)
Mg I	0.48 ± 0.34 (1)	−0.36 ± 0.38 (1)	0.22 ± 0.23 (2)
Si I	<1.70	<1.01	<1.76
Ca I	−0.03 ± 0.20 (3)	−0.01 ± 0.10 (9)	0.18 ± 0.10 (6)
Sc II	−0.01 ± 0.15 (5)	−0.20 ± 0.24 (8)	0.10 ± 0.15 (4)
Ti I	0.65 ± 0.17 (4)	−0.08 ± 0.15 (8)	0.11 ± 0.18 (3)
Ti II	0.29 ± 0.07 (24)	0.04 ± 0.07 (30)	0.39 ± 0.08 (20)
V I	0.72 ± 0.34 (1)	−0.26 ± 0.38 (1)	···
Cr I	−0.82 ± 0.17 (4)	−0.47 ± 0.08 (7)	−0.34 ± 0.16 (4)
Mn I	−0.72 ± 0.24 (2)	−0.81 ± 0.18 (3)	−0.33 ± 0.23 (2)
Co I	<1.11	<0.31	−0.26 ± 0.23 (2)
Ni I	0.36 ± 0.34 (1)	0.18 ± 0.13 (7)	0.35 ± 0.18 (3)
Cu I	<0.37	< −0.43	<0.39
Zn I	<0.66	<0.01	<0.77
Sr II	−1.56 ± 0.24 (S)	···	−1.21 ± 0.32 (S)
Y II	< −0.05	< −0.69	< −0.12
Zr II	<0.24	< −0.41	<0.36
Ba II	−1.07 ± 0.34 (S)	−1.12 ± 0.27 (S)	−0.98 ± 0.18 (S)
La II	<1.77	<1.15	<1.75
Nd II	<0.99	<0.34	<1.09
Eu II	<1.85	0.13 0.38 (1)	<1.90

Notes. We calculate [X/Fe] = [X/H] − [Fe I/H]. For Fe I, the abundance listed is 12 + log(Fe/H).
[a] A correction of Δ[Na/Fe] = −0.6 has been applied to account for NLTE effects on the Na D lines (Andrievsky et al. 2007). Similarly, we apply a correction of Δlog (Mn/H) = +0.5 to the Mn I resonance lines to account for NLTE effects (Bergemann & Gehren 2008).

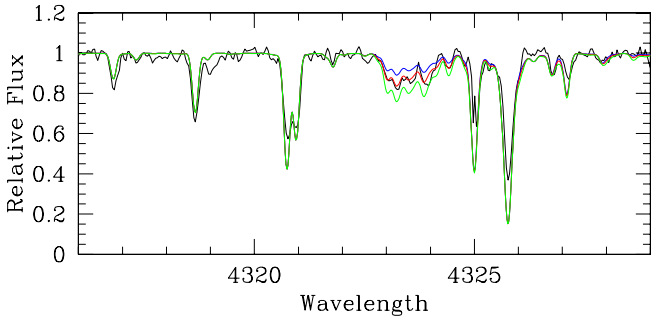

Figure 7. Spectrum synthesis of the CH 4320 Å feature in M68-6023. The chemical composition determined in this paper was used for the syntheses, along with three carbon abundances, [C/Fe] = −0.4, −0.6, −0.8. Broadening parameters were initially taken from the resolution of the Magellan spectra (Gaussian FWHM ∼ 0.15) and checked against the best-fit well-defined iron features.

(A color version of this figure is available in the online journal.)

carbon abundance from the CH line list by Brown et al. (1987) and Carbon et al. (1982), with acceptable fits as the abundance uncertainty. A C^{12}/C^{13} ratio of six was adopted (the typical value for bright RGB stars that have undergone the first dredge-up); this ratio made only a small difference such that increasing the value to 50 caused Δlog(C/H) = 0.06. Similarly, reducing the oxygen abundance had only a small effect (since C can be locked into the CO molecule); we adopted [O/Fe] = +0.4, but reducing this by 3× lowered the carbon abundance by only ⩽0.05 dex. The spectrum of M68-6023 around the CH 4320 Å feature is shown in Figure 7, with spectrum syntheses for three carbon abundances.

The carbon abundances for the M68 stars are in good agreement with typical red giants in globular clusters above the RGB bump (e.g., Smith et al. 2005; Gratton et al. 2000), where [C/Fe] ∼ −0.4 at the RGB bump and slowly decreases to ∼ − 1.0 dex at the RGB tip due to mixing of CNO-cycled gas. This trend can be seen in Figure 8 (lower panel, data from Gratton et al. 2000). The carbon abundances compiled by Frebel (2010) suggests a much larger scatter in carbon in metal-poor stars than seen in clusters (Figure 8, upper panel), however Frebel's compilation includes field stars of all evolutionary stages, including carbon-enhanced metal-poor (CEMP) stars. CEMPs have [C/Fe] > 1.0 and are thought to be both stars that have undergone mass transfer in a binary system with an AGB companion (CEMP-s, e.g., Beers & Christlieb 2005) and stars with high primordial carbon (e.g., from high-mass rotating stars; Meynet et al. 2006). Aoki et al. (2007) suggested that mixing on the RGB and extra mixing at the tip of the RGB will lower the surface carbon abundance, such that the definition of a CEMP star should depend on luminosity. This luminosity dependent range is shown in Figure 8 (lower panel), and clearly shows that stars in M68 and the Carina dSph are not CEMP stars by any definition.

The mean carbon abundance in M68 is ⟨[C/Fe]⟩ = −0.7 ± 0.1, in agreement with typical upper RGB stars. Upper limits on the carbon abundances in the metal-poor Carina stars are even lower ([C/Fe] ⩽ −1.0); this value is typical of upper RGB stars in globular clusters, but on the low side of the values found for the bright, metal-poor *field* stars in the Galaxy, as seen in Figure 8.

4.4.2. α-elements

The α-elements (O, Mg, Si, Ca, and Ti) are built from multiple captures of He nuclei (α particle) during various stages in

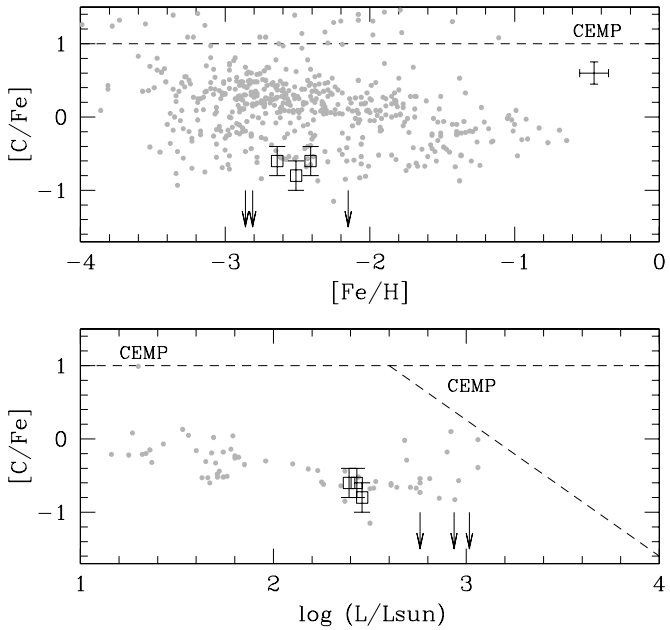

Figure 8. Carbon abundances in Galactic stars (small gray dots; Frebel 2010; Gratton et al. 2000), the three stars in M68 (empty black squares), and upper limits on the three metal poor Carina stars (upper panel). CEMP stars are usually defined as having [C/Fe] > 1.0, although extra mixing at the RGB tip can lead to a luminosity dependence as noted in the lower panel. The low carbon abundances in the Carina stars are consistent with those of luminous RGB stars in globular clusters (data from Gratton et al. 2000), which are not similar to CEMP stars.

the evolution of massive stars (>8 $M_{\odot}$, e.g., carbon burning, neon burning, and complete and incomplete Si burning) and dispersed during SN II events. Thus, the [α/Fe] ratio in a star is a way to trace the relative contributions from SN II to SN Ia products in the interstellar medium (ISM) when it formed (the nucleosynthesis of iron is discussed in the next section). Although Ti is not a true α-element, the dominant isotope ^{48}Ti forms through explosive Si burning and the α-rich freezeout,[20] thus it behaves like an α-element (Woosley & Weaver 1995).

Our [α/Fe] results are plotted in Figures 9 and 10. Koch et al. (2008a) determined α-element abundances for four stars in common with ours, and a solid line connects those results in the figures. In general, the α-element abundances in Carina tend to be lower than the Galactic distributions at all intermediate metallicities, i.e., $-2.2 < [Fe/H] < -1.3$. In the most metal-poor stars at [Fe/H] = −2.9, most of the α-elements are in good agreement with the Galactic distributions. Two stars stand out in their [α/Fe] distributions, Car-612 and Car-5070, which have very low ratios of [Mg, Ca, and Ti/Fe] for their metallicities. These two stars will be discussed further in the following sections.

Oxygen. Oxygen abundances in this analysis are solely from the [O I] 6300 line. Oxygen could only be measured in the higher metallicity stars in the sample where the line is stronger. Excellent agreement was found for one star in common with Koch et al. (2008a; Car-484, where they found [O/Fe] = +0.39 and we find = +0.48).

Silicon. Silicon abundances are only available for the higher metallicity stars. Line measurements of the Si I lines at 5684 Å and 6155 Å are similar to those in Koch et al. (2008a), however

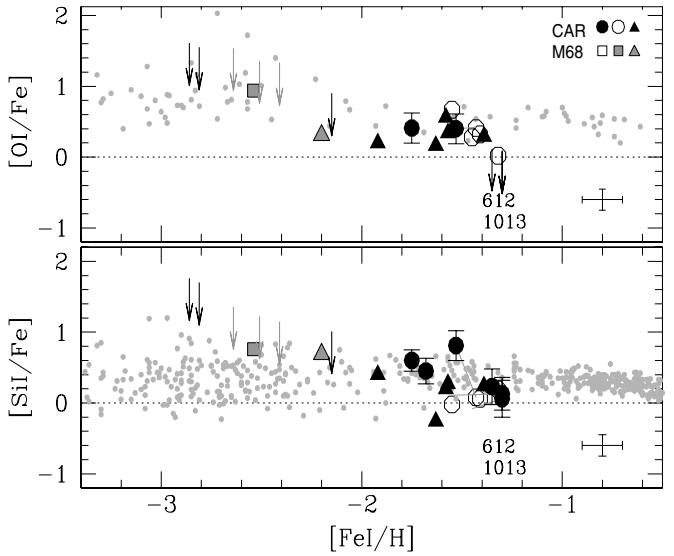

Figure 9. LTE oxygen and silicon abundances of stars in Carina and M68, compared to the Galactic distribution. Results for Carina are from this paper (filled circles), Koch et al. (2008a; empty circles), and Shetrone et al. (2003; filled triangles); for four stars in common between this analysis and Koch et al., the abundance results are connected by a gray line. M68 results are shown for one star from Shetrone et al. (2003; gray triangle) and the mean of seven RGBs from Lee et al. (2005; gray square). Usually our M68 results are shown by empty black squares, but for O and Si only upper limits are available, shown as gray arrows. A representative error bar is shown (Δ[Fe/H] = ±0.1, Δ[X/Fe] = ±0.15), although the actual errors per star from this analysis are also plotted per point. Small gray points show the Galactic distributions summarized by Venn et al. (2004) and Frebel (2010).

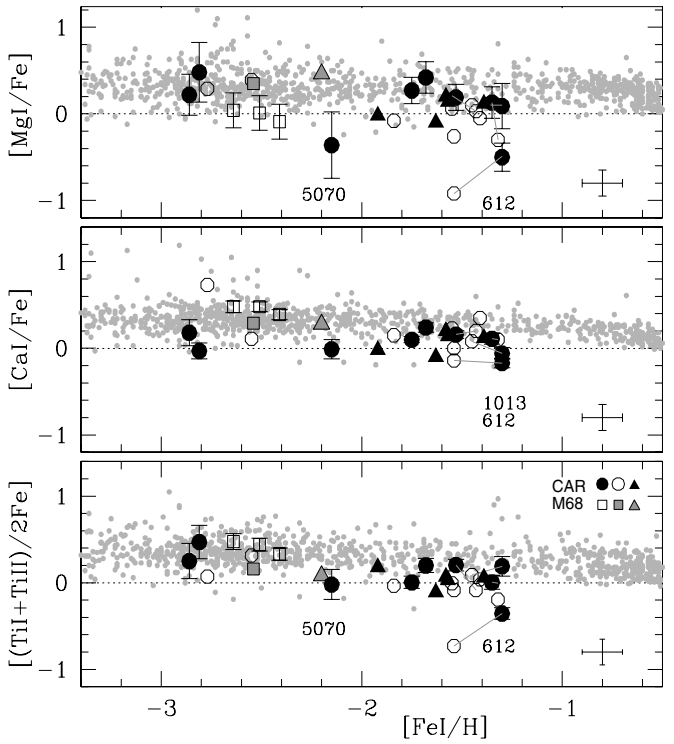

Figure 10. LTE magnesium, calcium, and titanium abundances of stars in Carina and M68, compared to the Galactic distribution. Symbols are the same as in Figure 9.

our oscillator strength for one line is lower by 0.4 dex. Only upper limits were available from the Magellan spectra taken of the metal-poor stars.

[20] The α-rich freezeout occurs when a strong shock travels through infalling matter at the inner most shell of a core-collapse supernova. After being shocked, material is heated to >5 billion degrees, so that nuclei decompose into neutrons and tightly bound α particles.

Magnesium. Mg I abundances were calculated from the λ5528 line in all of the Carina stars, combined with λ5172 and λ5183 when <200 mÅ, and λ5711 in the FLAMES/UVES spectra (it was too weak to measure in the Magellan spectra). The abundances between these lines are in good agreement. We note that the Carina Mg abundances are in good agreement with those from Koch et al. (2008a) and Shetrone et al. (2003); see Figure 10.

Calcium. Many lines of Ca I were available in all of the program stars, over a wide range of wavelengths, and of appropriate line strengths. Results are in good agreement with Koch et al. (2008a); see Figure 10.

Titanium. Titanium abundances were determined from a range of Ti I and Ti II lines across the entire spectral region. The abundances between the two species are in good agreement, typically within 1σ of each other, despite the possibility that titanium can be overionized by the radiation field resulting in lower Ti I abundances when LTE is assumed. Letarte et al. (2010) suggested that better agreement is found when [Ti I/Fe I] is compared to [Ti II/Fe II] in their sample of Fornax RGB stars, due to similarities in the NLTE effects and possibly due to temperature scale variations. Examination of our M68 comparison stars are in agreement with their finding, such that the agreement improves when Ti II is compared with Fe II; however this had no effect on our Carina abundances. Thus, in this paper, the abundances from both species are averaged together. We note that our Carina Ti abundances are in good agreement with those from Koch et al. (2008a) and Shetrone et al. (2003); see Figure 10.

4.4.3. Sodium

Sodium is produced primarily during the carbon burning stages, but as metallicity increases a sufficient amount of neutron-rich material also allows sodium to be produced through the Ne–Na cycle during H burning (Woosley & Weaver 1995). Thus, the chemical evolution of Na initially follows the α-elements, but then deviates from this (rising) when AGB stars contribute. Furthermore, Herwig (2004) have shown that *metal-poor AGB stars* from 2 to 5 $M_{\odot}$ will *overproduce* sodium by factors of 10–100. This Na overproduction has multiple sites dependent on the AGB mass.

In the FLAMES/UVES spectra, sodium abundances were determined from a single Na I line at 5688 Å; this was because the resonance Na D lines at 5895 and 5889 Å were too strong (∼300 mÅ), and the line at 5682 Å (used by Koch et al. 2008a) was too weak. Only the most metal-poor stars in Carina have Na D lines that are weak enough to be used in this analysis, but since those stars were observed with Magellan/MIKE spectra, their lower S/N spectra required spectrum syntheses for the line abundance determinations. The Fe I 5615 and 5634 lines were examined to check the broadening parameters (Gaussian broadening with FWHM = 0.25 Å was adopted, which is the effective resolution of the Magellan MIKE spectra). When the Na D lines could not be fit simultaneously, then an average of the best-fit abundances for each line was adopted, and the range used to estimate the uncertainty.

Andrievsky et al. (2007) have examined the NLTE corrections for the Na D resonance lines in metal-poor RGB stars. Using their Table 2, combined with their Figure 6 showing the effect of the correction on the line EWs, then we estimated an NLTE correction for our abundances. For the M68 stars, the higher gravities and strong line strengths imply corrections of ∼−0.5 dex. For the three metal-poor Carina stars (Car-1087, Car-5070, and Car-7002), the atmospheric parameters and line strengths suggest corrections of ∼−0.6 dex. These corrections are included in Figure 11. Of course, no corrections are applied to the other Carina objects since we did not use the Na D lines for those.

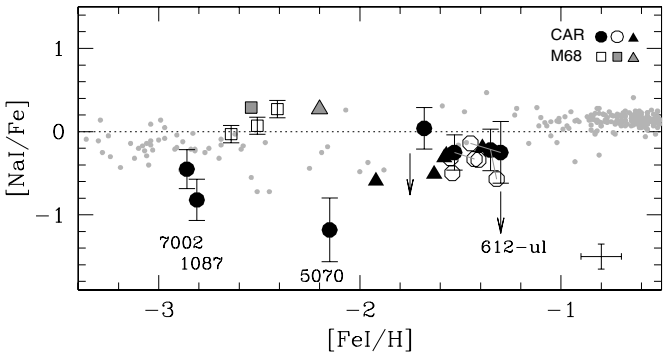

Figure 11. Sodium abundance ratios of stars in Carina and M68, compared to the Galactic distribution. For the metal-poor stars in Carina and M68, NLTE corrections have been applied to the Na D line abundances; the symbols are the same as in Figure 9. For the Galactic data, only a limited amount of available data is shown; the results from Andrievsky et al. (2007) and Gehren et al. (2006) are included since these two studies considered NLTE effects on the NaD lines, and results from Reddy et al. (2003, 2006) are shown since they only used the subordinate Na I lines.

For Car-612, we only determined an upper limit, EW < 30 mÅ for Na I λ5688, which corresponds to a very low upper limit of [Na/Fe] = −0.8. This result is comparable to that from Koch et al. (2008a), who measured an EW (=24 mÅ) for the same weak line and determined [Na/Fe] = −0.5. Our lower upper limit is due to small differences in the atmospheric parameters and adopted solar Na abundance.

4.4.4. Iron-peak Elements

In the early universe, the iron-peak elements (Sc to Zn: $23 \leqslant Z \leqslant 30$) are exclusively synthesized during Type II supernovae explosions by explosive oxygen and neon burning, and complete and incomplete explosive Si burning. Abundances of these elements show a strong odd–even effect (odd nuclei have lower abundances than the even nuclei). Their yields depend on the mass of the progenitors (e.g., Woosley & Weaver 1995), the mass cut adopted (mass expelled relative to the mass that falls back onto the remnant, e.g., Nakamura et al. 1999), and SNe II explosive energies (e.g., Umeda & Nomoto 2005; Heger & Woosley 2002). Only at later times (∼1 Gyr, e.g., Maoz et al. 2010), when lower mass stars reach the end of their life time, do SNe Ia become a significant, possibly the dominant, contributor to the total iron-group inventory. The onset of SNe Ia in the chemical evolution of the Galaxy is observed as a *knee* in the [α/Fe] versus [Fe/H] near [Fe/H] ∼ −1.0 (e.g., McWilliam et al. 1995). At lower metallicities, SNe Ia [X/Fe] yields could vary (e.g., Kobayashi & Nomoto 2009). We have measured several of the Fe-peak elements in the Carina stars to compare with the Galactic trends.

Scandium. Several (4–13) lines of Sc II were measured and HFS corrections applied. The distribution in the Sc abundances at intermediate metallicities is larger than most of the other iron-peak elements (see Figures 12 and 13), although this includes Car-612, which has several chemical peculiarities and stars analyzed by Shetrone et al. (2003). Other than those objects, the Sc abundances are similar to the Galactic distribution.

Vanadium. For most of the intermediate-metallicity stars, the V abundance is well determined from ∼10 V I lines and HFS

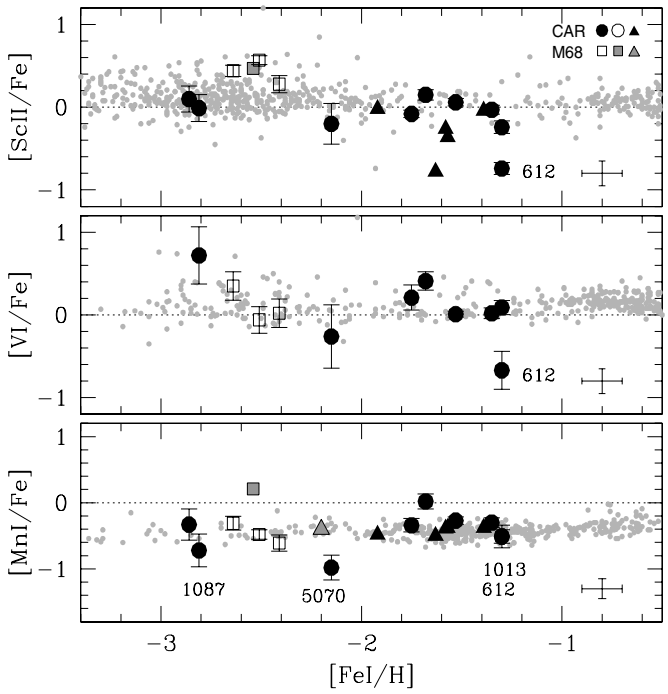

Figure 12. Odd-*Z* LTE abundance ratios for scandium, vanadium, and manganese in Carina. HFS corrections have been applied, as well as a NLTE correction to the resonance lines of Mn I. Symbols are the same as in Figure 9 with the exception of the Galactic standards for [Mn/Fe], which are taken from Sobeck et al. (2006) and Cayrel et al. (2004).

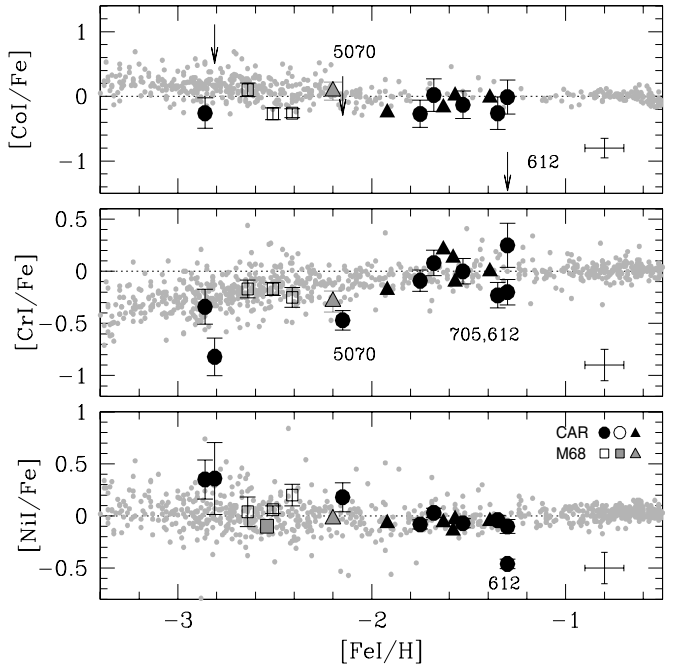

Figure 13. LTE abundance ratios for chromium, cobolt, and nickel in Carina. The low abundances for Car-612 and low Cr in Car-5070, are exceptional, as in Figure 12. Symbols are the same as in Figure 9.

corrections were applied. However, in the metal-poor stars and Car-612, it is determined from only 1–2 lines.

Manganese. The Mn I abundances were determined from several lines (4–7) in the intermediate-metallicity stars, and these line abundances showed good agreement with one another. Generally, [Mn/Fe] in Carina follows the Galactic distribution above [Fe/H] = −2. In the metal-poor Carina stars and M68 stars, a different set of spectral lines was used (because of the wavelength coverage and resolution of the Magellan/MIKE spectra). The blue resonance lines at λ4030, 4033, and 4034, as well as several additional subordinate lines were measured, with only λ4823 in common between the MIKE/Magellan and FLAMES/UVES data sets. The Mn results from the resonance lines were lower than from λ4823 and the other subordinate lines in the M68 standard stars, most likely due to non-LTE effects. Bergemann & Gehren (2008) have calculated non-LTE corrections for Mn I lines and do find large corrections for the blue resonance lines that are metallicity dependent. They do not give corrections for red giants, but for red main-sequence stars the corrections can be as large as +0.5 dex at [Fe/H] = −3. These corrections are similar to the offsets that we find between resonance and subordinate lines, therefore we apply a correction of Δlog(Mn) = +0.5 dex to the Mn I resonance line abundances—this correction should be checked with proper modeling of these metal-poor red giant atmospheres. Correcting the resonance line abundances improves the mean [Mn/Fe] results, but the mean values in Car-5070 and Car-1087 remain lower than for similar stars in the Galactic halo.

Chromium. Cr abundances were determined from 4–7 lines of Cr I, which showed good agreement from line to line. A recent calculation of the NLTE effects on the Cr I lines by Bergemann & Cescutti (2010) showed that the corrections are small (⩽0.1 dex), but that Cr I/Cr II ionization equilibrium and the solar [Cr/Fe] ratio is regained for metal poor stars, rather than the downward trend seen in Figure 13. Our Carina data generally follow the Galactic trend, with the exception of very low abundances in Car-5070, Car-1087, Car-705, and Car-612.

Cobalt. Co was determined from only 1–2 lines in this analysis. The [Co/Fe] ratios lie slightly below the Galactic abundances, although they are not well constrained from so few lines. The only exception is the very low upper limit to [Co/Fe] for Car-612 (see Figure 13). Bergemann et al. (2010) calculated NLTE corrections for Co I and Co II; they suggest the NLTE corrections depend on metallicity and can become as large as +0.6 to +0.8 dex at [Fe/H] ∼ −3.0. This would not affect the very low Co upper limit found for Car-612.

Nickel. Several Ni I lines (13–17) were measured in the intermediate-metallicity stars over a range of wavelengths, showing that [Ni/Fe] is in agreement with the Galactic distribution (Figure 13). Only 1–3 Ni I lines were available in the most metal-poor stars though, thus the uncertainties are large because σ(Fe I) was adopted for the error estimates. Only the Ni result for Car-612 stands out, but this result is robust, determined from 14 Ni I lines with a small error in the mean. Combined with the low Na upper limit, then Car-612 fits the Na–Ni relationship observed for some α-poor stars in the Galaxy by Nissen & Schuster (1997, 2010).

4.4.5. Cu and Zn

While contiguous on the periodic table, the main nucleosynthetic sites of copper and zinc are difficult to ascertain. In massive stars, Cu and Zn form during complete Si burning, the α-rich freezeout, and even the weak *s*-process (e.g., Timmes et al. 1995). The contributions to the production of Cu and Zn in AGB stars are uncertain, though recent calculations suggest that small amounts of Cu and even smaller amounts of Zn can be produced in more massive (5 $M_{\odot}$) AGB stars (Karakas et al. 2008; Karakas 2010). Precise estimates of the AGB yields can also depend on uncertain parameters such as the mass-loss law and number of dredge-up episodes (Travaglio et al. 2004). The majority of these

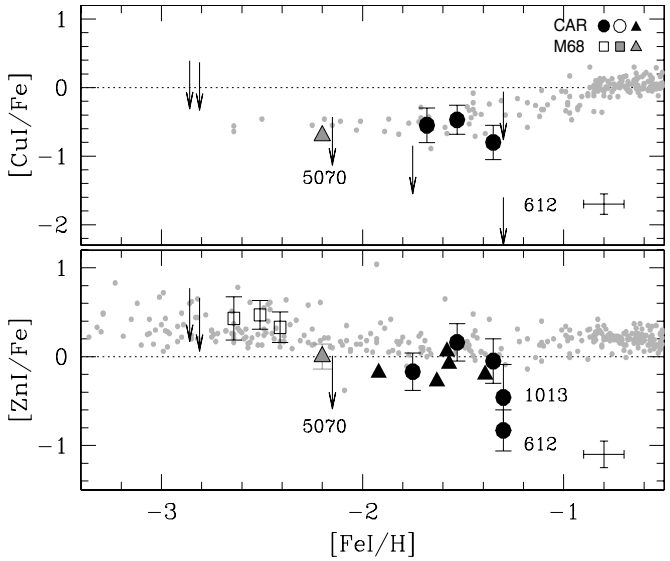

Figure 14. LTE copper and zinc abundances in the Carina stars. The Cu and Zn abundances in Car-612 are remarkably low. Symbols are the same as in Figure 9.

elements are thought to form in SN Ia events though, where the yields of Cu and Zn are sensitive to the neutron excess and thus metallicity (Matteucci et al. 1993; Mishenina et al. 2002; Travaglio et al. 2005; Kobayashi & Nomoto 2009).

Copper. The Cu I line at 5105 Å was observed in some of our target stars. Upper limits were calculated adopting an EW of 30 mÅ for the FLAMES/UVES spectra and 50 mÅ for the most metal-poor Carina stars. HFS corrections were applied. Generally, copper follows the Galactic trend, and though we have very few actual measurements, the upper limit for Car-612 is very low and provides a very strong constraint.

Zinc. The Zn I line at λ4810 was observed in most of our sample, or used to determine the upper limits to the Zn abundance (adopting <40 mÅ); see Figure 14. The zinc abundances at intermediate metallicities were slightly lower than the Galactic distribution, especially Car-612.

4.4.6. Neutron-capture Elements

Neutron-capture elements (Sr to U, $38 \leqslant Z \leqslant 92$) originate in the rapid neutron-capture process (*r*-process) that occurs during explosive nucleosynthesis in SNe II. The *r*-process has a *main* source in 8–10 $M_{\odot}$ stars that form elements with $Z > 50$, and a *weak* source in more massive progenitors (>20 $M_{\odot}$) that contribute primarily to the lighter neutron-capture elements (e.g., Sr, Y, Zr; Travaglio et al. 2004). A more detailed examination of the *r*-process shows that a more accurate representation is in terms of a high entropy wind model (Farouqi et al. 2009; Roederer et al. 2010); nucleosynthesis in low entropy winds proceeds primarily through a chared-particle (α-) process, whereas a neutron-capture component (the classical weak and main *r*-processes) occur in the high entropy winds. Thermal pulsing in AGB stars also contributes to these elements through the slow neutron-capture process (*s*-process). With intermediate masses (2–4 $M_{\odot}$), AGB stars have longer lifetimes than the sites of the *r*-process, and therefore in simple chemical evolution models AGB stars do not produce any of the heavy elements in the most metal-poor stars, but dominate the formation of some of these elements at later times and higher metallicities. In the Galaxy, this is seen as the *rise in the s-process* that begins near [Fe/H] = −2.5 (McWilliam 1998; Burris et al. 2000; François et al. 2007); this is in contrast to the knee in [α/Fe] due to contributions from SNe Ia near [Fe/H] = −1.0. In the Sun, the *r*-process contributes 11%, 15%, 25%, 28%, 53%, and 97% of Sr, Ba, La, Y, Nd, and Eu, respectively (Burris et al. 2000). Thus, Eu is critically important as a nearly pure *r*-process indicator.

Yttrium. [Y/Fe] in the intermediate-metallicity stars was determined from Y II 4883, 5087, and 5200, which gave very consistent abundances from line to line and star to star. The Y II 4900 line could not be used because it is severely blended in all of the spectra. The [Y/Fe] ratios are similar to those found by Shetrone et al. (2003), i.e., slightly below the Galactic values at intermediate metallicities; see Figure 15. One exception is Car-612, which has an extremely low [Y/Fe] result, and another is Car-5070, which has a low upper limit value. The low [Y/Fe] in Car-612 can be seen directly in comparison with Car-705—Figure 16 shows that the Fe I line strengths are similar but the Y II 5087 line is much weaker in Car-612. Upper limits were determined in the most metal-poor stars using 40 mÅ as the EW upper limit for the Y II λ4883 line.

Barium. Five lines of Ba II were analyzed (at 4554, 4934, 5853, 6141, and 6496 Å), which yielded consistent abundances from line to line and star to star, although they were not all observed in one star. Spectrum syntheses were used to confirm the abundances when the S/N was low. HFS corrections for three lines (5853, 6141, and 6496 Å) are negligible (⩽0.02). NLTE corrections are also negligible (⩽0.03, Short & Hauschildt 2006), with the exception of the λ4554 resonance line, however we have chosen to *not correct* that line since the estimated correction is not large (⩽0.15 dex, Short & Hauschildt 2006; Andrievsky et al. 2009) and the LTE abundance from that line is consistent with the other Ba II line results. Most stars in Carina have the same [Ba/Fe] distribution as stars in the Galaxy, with the exception of three stars, Car-612, Car-5070, and Car-705; see Figure 15.

Lanthanum. La was determined from three lines of La II at λ6320, 6390, 6774 (additional lines at λ4333, 5301, 5303 could not be used due to the S/N of the spectra). Negligible HFS (⩽0.02) were calculated for two La lines (λ6320 and 6390). [La/Fe] follows the Galactic distribution for the few stars where we could measure it (see Figure 15).

Strontium. [Sr/Fe] was determined from two Sr II lines at very blue wavelengths (4077 and 4215 Å) reached only by our Magellan/MIKE spectra. The S/N is poor in that region, thus we adopted the results from spectrum syntheses for those lines in the three Carina stellar spectra; see Figure 17. Nevertheless, the interpretation of the synthetic results remains difficult; the λ4077 line is the stronger of the Sr II resonance lines, and yet the detection of the λ4215 line is more clear in Car-7002, and possibly Car-1087. The best estimates for the Sr abundances in these two stars are listed in Table 13. An Sr upper limit for Car-5070 could not be determined due to noise near both the λ4215 and 4077 lines. NLTE corrections were considered, but not applied to our results. Short & Hauschildt (2006) estimate abundance corrections of −0.07 dex, whereas Andrievsky et al. (2011) estimate corrections of ∼0.0 and +0.1 dex for λ4077 and 4215, respectively. We chose to not apply either correction since these estimates are small and in opposite directions.

Zirconium. Upper limits for Zr were determined from the Zr II λ4208 line in the Magellan spectra. These upper limits are quite high and do not add the discussion on the heavy element abundances.

Neodymium. Nd was determined from two Nd II lines (λ5319 and 5249) for all stars with FLAMES/UVES spectra, and these

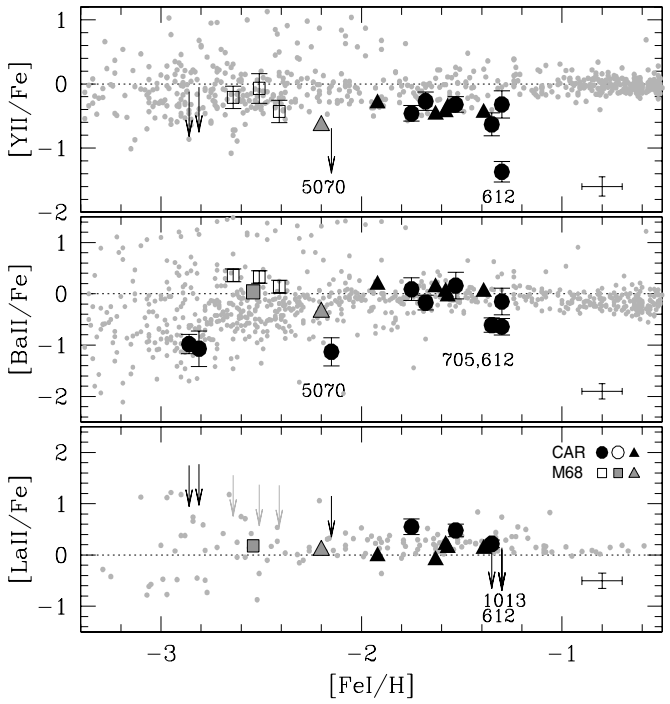

Figure 15. LTE abundances for the heavy elements Y, Ba, and La in Carina and M68, compared to the Galactic distribution. The Y abundance in Car-612 is remarkably low, but verified by a comparison of the spectra of Car-612 and Car-705, e.g., in Figure 16. The Galactic star abundances for La are from the critically examined compilation by Roederer et al. (2010). These ratios are again quite low for Car-612 and Ba in Car-5070. Symbols are the same as in Figure 9.

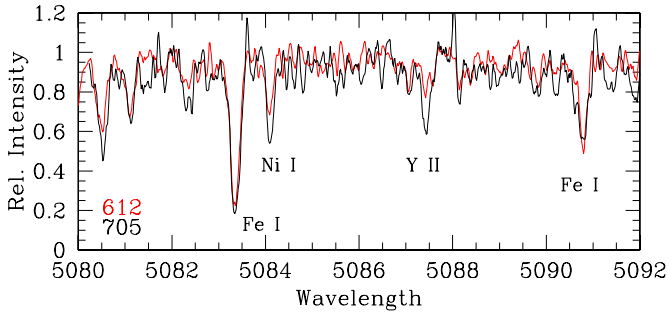

Figure 16. Spectra around the Y II 5087 Å lines in Car-612 and Car-705. Since the atmospheric parameters and metallicities of these two stars are very similar, then this figure shows yttrium is truly weaker in Car-612. Spectrum synthesis in this region confirms the different Y II abundances derived from the EW analyses. The lower [Ni/Fe] abundances in Car-612 can also be seen directly by comparing the 5084 Å lines.

(A color version of this figure is available in the online journal.)

lines were used to calculate the upper limits from the Magellan spectra. Nd is consistent with the Galactic distribution, though it is very low in Car-612 (Figure 18).

Europium. The europium abundance in the Sun is nearly entirely due to the *r*-process, therefore Eu is identified as an important indicator in any stellar analysis to establish the ratio of *r*-process to *s*-process contributions of the neutron-capture elements. In this analysis, three Eu II lines were examined (λ4129, 4205, and 6645). Unfortunately, all three lines were not observed in any one star; the Magellan spectra have too low resolution to detect the weak 6645 Å line, and the FLAMES/UVES data do not cover the bluer wavelengths. Nevertheless, the Eu results are consistent with the Galactic distribution (see Figure 18). HFS and isotopic splitting corrections are negligible (<0.05 dex).

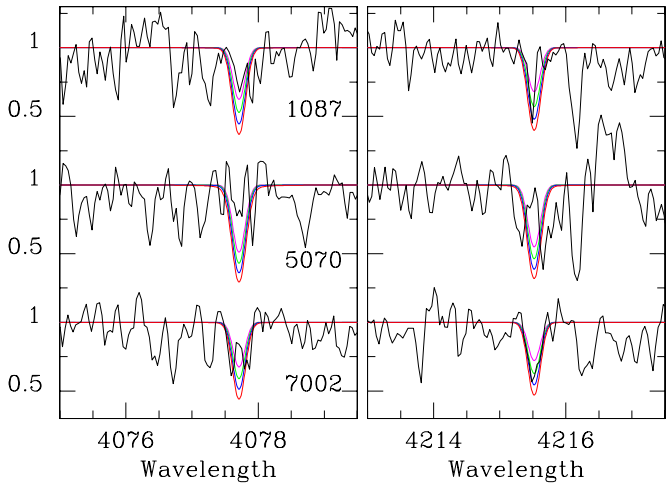

Figure 17. Spectrum syntheses of the Sr II 4077 and 4215 lines in the three most metal-poor Carina stars, for [Sr/Fe] = −0.5, −1.0, −1.5, and −2.0. The low S/N makes accurate Sr abundances very difficult.

(A color version of this figure is available in the online journal.)

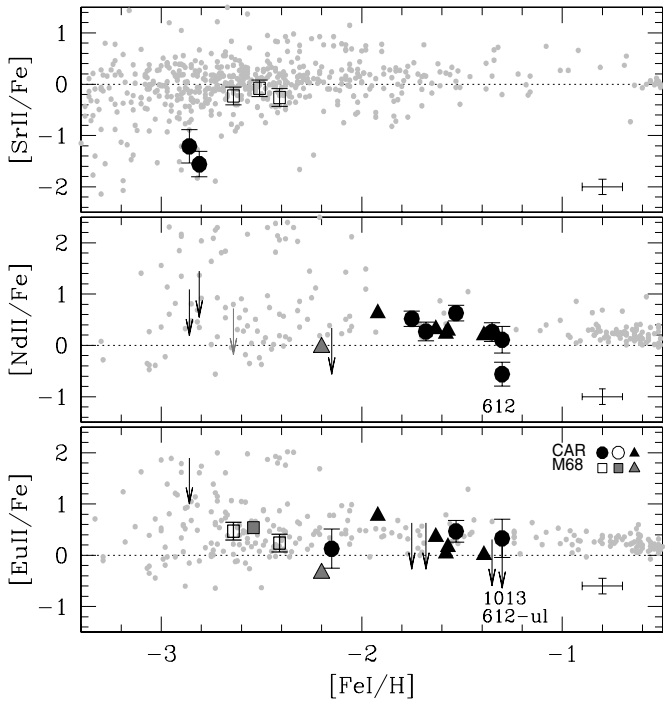

Figure 18. LTE abundances for the heavy elements Sr, Nd, and Eu in Carina and M68, compared to the Galactic distribution. Symbols the same as in Figure 9.

4.4.7. s-process to r-process Ratios: [X/Eu]

To assess the relative amounts of *s*-process to *r*-process contributions among the neutron-capture elements, then abundance ratios relative to Eu are examined. In Figure 19, [Y/Eu] and [Ba/Eu] of stars in Carina and the Galaxy are shown and compared to the solar *r*-process fractions from Burris et al. (2000; also see Arlandini et al. 1999). In both [Y/Eu] and [Ba/Eu] (as well as [La/Eu] and [Nd/Eu], not shown), the gradual rise in these ratios can be seen with increasing metallicity. McWilliam (1998) showed that the rise in the *s*-process starts at [Fe/H] = −2.5 in the Galaxy. In Carina, this rise appears to begin at a higher metallicity, [Fe/H] ⩾ −2.0. This is most likely due to the metallicity dependence of the AGB yields, as modeled by Travaglio et al. (2004; also Pignatari et al. 2010), where fewer

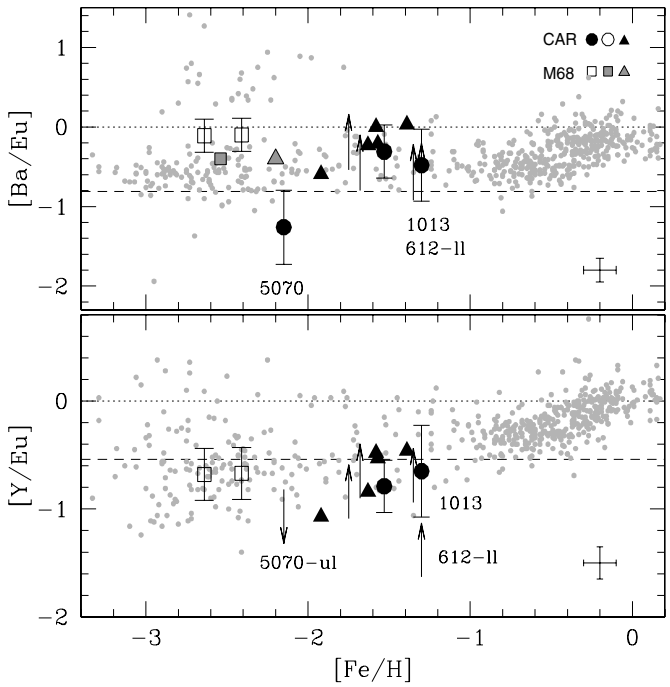

Figure 19. Neutron-capture ratios with Eu of stars in Carina and M68, compared to the Galactic distribution. The ratio with Eu permits an assessment of the *s*-process contributions relative to the *r*-process contents in the Sun (Burris et al. 2000; dashed line). The rise in the *s*-process can be seen in the Carina stars and the Galactic distributions. Upper and lower limits are shown for some stars. Symbols are the same as in Figure 9.

iron seed nuclei in a high neutron density wind can collect more neutrons, thus underproducing the first *s*-process peak elements,[21] and overproducing the second and/or third *s*-process peak elements. The slightly lower [Y/Eu] and slightly higher [Ba/Eu] ratios in Carina are consistent with metal-poor AGB stars contributions.

As a final note, the high Ba abundance in M68 is somewhat surprising. This was also found by Lee et al. (2005). Since [Ba/Eu] is high, but [Eu/Fe] is normal, this suggests M68 has had an unusual chemical evolution, possibly having been enriched (or self-enriched) by metal-poor AGB stars.

5. DISCUSSION

Detailed chemical abundances for up to 23 elements in nine stars in the Carina dSph have been presented in this paper. Previously, only five stars in this dSph had detailed abundance determinations for so many elements (Shetrone et al. 2003), while another ten had [α/Fe] determinations from high-resolution spectroscopy (Koch et al. 2008a). In a companion paper by Lemasle et al. (2012), the VLT FLAMES/GIRAFFE spectra for 36 additional RGB stars are presented, but due to the limited wavelength coverage of those spectra, only four elements are analyzed in detail (Mg, Ca, Ba, and Fe). For the first time, Lemasle et al. (2012) calculated the ages of all stars with detailed chemical abundances in the Carina dSph, including those in this paper, from isochrone fitting. While the uncertainties in the ages can be quite large for any one star, the differential ages should be better, and any discussion regarding ages is therefore limited to two age bins, an *old* population and an *intermediate-aged* population. These ages (two age bins) are adopted in this discussion.

In the previous section, our results were compared to stars in the Galaxy, where some chemical peculiarities were noted. In this section, we will compare our abundance results to those of stars in other dwarf galaxies. Three dSphs have been chosen for comparison: Sculptor, Fornax, and Sextans. The data sets for the three dSphs are taken from Shetrone et al. (2001, 2003), Geisler et al. (2005), Aoki et al. (2009), Letarte et al. (2006, 2010), Tafelmeyer et al. (2010), and Frebel et al. (2010a), all scaled to the Asplund et al. (2009) solar abundances. These three dSphs were chosen since large data sets of detailed abundances from high-resolution spectroscopy are available, and the analyses of those spectra used similar methods and model atmospheres to our analysis. We do not include results from Kirby et al. (2009, 2010, 2011a, 2011b) in these comparisons to avoid systematic differences due to the lower resolution of their spectra and differences in the analysis methods. Also, we do not include higher mass dwarfs (e.g., the LMC, SMC, or Sgr) because the metallicity range of the stars in those galaxies do not overlap well with the stars in the Carina dSph.

We also compare several elemental abundances of the most metal-poor stars in Carina to stars in the UFD galaxies and the metal-poor stars in the Draco dSph. Data sets for the UFDs are from the compilation by Frebel (2010), and for Draco are from Cohen & Huang (2009), Fulbright et al. (2004), and Shetrone et al. (2001). These comparisons are valuable because Carina has a tiny dynamical mass within its half-light radius ($M_{1/2}$), e.g., $M_{1/2}$ (Carina) $= 6.1 \pm 2.3 \times 10^6\ M_\odot$ (Walker et al. 2009), which is a factor of 2, 4, and 9 times smaller than Sculptor, Sextans, and Fornax, respectively, but is comparable to those of the more massive UFDs. As an example, Böotes I has $M_{1/2} = 5.9 \pm 3.7 \times 10^6\ M_\odot$, which is essentially the same as Carina, although the masses of the UFDs continue to be revised downward, e.g., the mass of Boötes I has been revised downward by a factor of 14 due to the lower velocity dispersions found by Koposov et al. (2011). Of course, Carina is not considered an UFD because of its luminosity—Carina is 8× brighter than Boötes I (Walker et al. 2009).

5.1. The Metallicity Distribution of the High-resolution Spectroscopic Sample

As shown in Figure 4 of Lemasle et al. (2012), the stars that have been analyzed with high-resolution spectroscopy are biased toward metallicities near [Fe/H] $= -1.5 \pm 0.3$. This is the same as the mean metallicity and metallicity range predicted for the dominant IA population by Bono et al. (2010) from their CMD analysis; however this is not scientifically significant for two reasons. First, more than half of the high-resolution sample comes from the FLAMES/GIRAFFE spectral analysis presented by Lemasle et al. (2012), and as discussed in that paper, the low S/N of those spectra meant that the weaker lines of the more metal-poor stars were harder to detect. This effectively removed those stars from the analysis. Second, although the *V* magnitude at the tip of the RGB may be slightly brighter with higher metallicities, this is only a small effect and maximizing the fiber placement was a more significant concern. Also, while it is true that the three stars targeted for Magellan/MIKE observations are located in the outer fields of Carina and are the most metal-poor stars sampled, this does not imply a population gradient in Carina as those stars were purposely selected for their low metallicities. Koch et al. (2006) found no

[21] The *s*-process peaks are defined by the neutron magic numbers for filling nuclear shells (e.g., $N = 50$, 82, 126 are full nuclear shells). A full nuclear shell lowers the cross section for further neutron captures, thus elements collect at these neutron numbers defining the first, second, and third *s*-process peaks.

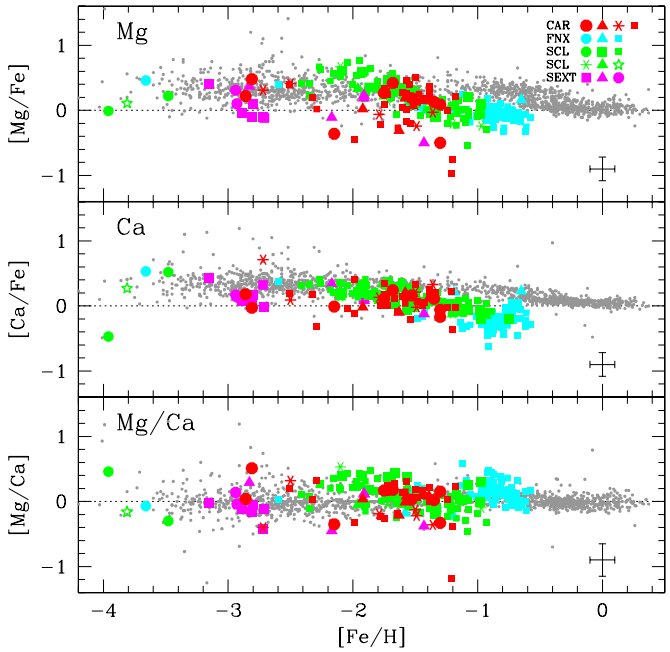

Figure 20. Mg and Ca abundances of stars in Carina (red), Sculptor (green), Fornax (cyan), and Sextans (magenta). Symbols for Carina: solid circles are from this paper, squares are from Lemasle et al. (2012), triangles are from Shetrone et al. (2003), and asterisks are from Koch et al. (2008a). Symbols for Fornax: circles are from Tafelmeyer et al. (2010), triangles are from Shetrone et al. (2003), squares are from Letarte et al. (2010). Symbols for Sculptor: large/small squares are UVES/GIRAFFE FLAMES data from V. Hill et al. (2012, in preparation), solid circles are from Tafelmeyer et al. (2010), asterisks are from Geisler et al. (2005), triangles are from Shetrone et al. (2003), and the star is from Frebel et al. (2010a). Symbols for Sextans: squares are from Aoki et al. (2009), triangles are from Shetrone et al. (2001), and circles are from Tafelmeyer et al. (2010). Tafelmeyer et al. (2010) note that the very low [Ca/Fe] ratio reported for the most metal-poor dSph star (at [Fe/H] ~ -4) is likely due to NLTE effects in the formation of the strong resonance Ca I 4227 Å line, a line that was not used throughout the rest of their analysis, and therefore should be regarded with caution. Representative error bars of Δ[Fe/H] $= \pm 0.1$ and $\Delta[X/\mathrm{Fe}] = \pm 0.15$ are shown.

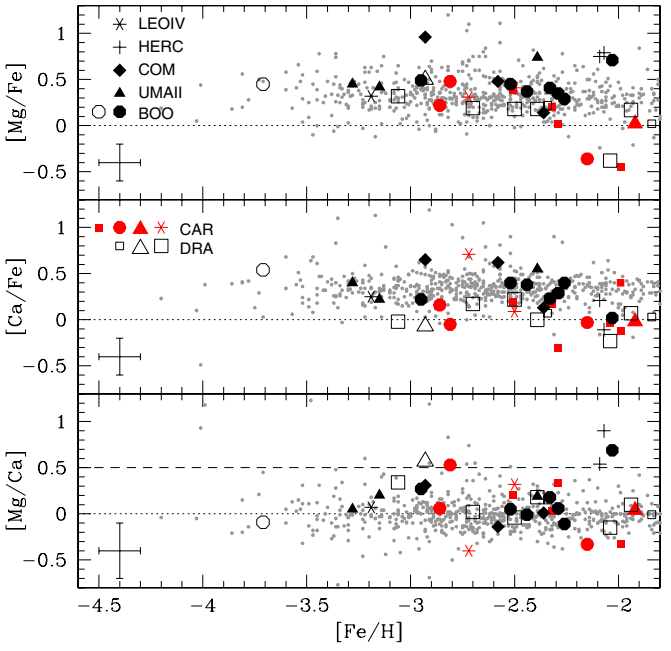

Figure 21. [Mg/Fe] and [Ca/Fe] in the most metal-poor stars in the Galaxy, Carina, Draco, and UFD galaxies. The data for Carina are the same as in Figure 20, while for Draco, the small/large squares are from Shetrone et al. (2001)/Cohen & Huang (2009). The large empty triangle is Draco-119, the metal-poor star found by Shetrone et al. (2001) and reanalyzed with higher S/N spectra by Fulbright et al. (2004). The UFDs are presented as follows: solid/empty circles are for Böotes I from Feltzing et al. (2009)/Norris et al. (2010b), solid triangles are for Ursa Major II from Frebel et al. (2010b), solid diamonds are for Com Ber from Frebel et al. (2010b), plus signs are for Hercules from Koch et al. (2008b), and the asterisk is for one star in Leo IV by Simon et al. (2010). The dashed line in the [Mg/Ca] panel represents stars with the more extreme enhancements (three in UFDs and two in dSphs).

significant difference in the mean metallicities of RGB stars in the inner and outer fields of Carina. Thus, the results presented in this paper are not used to constrain the distributions in location or metallicity of the stars in Carina.

5.2. Dispersions in [α/Fe]

In Figure 20, we show [Mg/Fe] and [Ca/Fe] for Carina, compared to the three other dSphs and the Galaxy, over the full metallicity range examined. Looking at [Ca/Fe] alone suggests that the chemical evolution of Carina has been similar to Sculptor. In Sculptor, a noticeable downward trend in these abundances begins at [Fe/H] ~ -1.8, whereas in Galactic stars this occurs at a higher metallicity. This knee in the [α/Fe] ratios is usually interpreted as the onset of contributions to [Fe/H] from SN Ia, with the shift in the knee to lower metallicities in dwarf galaxies attributed to their slower chemical evolution (e.g., Lanfranchi et al. 2008; Kirby et al. 2011a). In Carina, it is not clear where or if there is a knee.

The more remarkable result seen in Figure 20 is the dispersion in [Mg/Fe] (Δ[Mg/Fe]) in Carina, which is observed in both the FLAMES/UVES and FLAMES/GIRAFFE data, and is much larger than the dispersion in [Ca/Fe] (Δ[Ca/Fe]). A calculation of the intrinsic spreads[22] suggests that this difference is real and significant when considering the whole data set, the data from Lemasle et al. (2012) only, our nine UVES targets alone, or the data at a specific intermediate metallicity (such as [Fe/H] $= -1.2 \pm 0.1$), i.e., $0.4 \leqslant [N_i([\mathrm{Mg/Fe}]) - N_i([\mathrm{Ca/Fe}])] \leqslant 0.7$. Only for [Fe/H] < -2.0 are the intrinsic spreads between [Mg/Fe] and [Ca/Fe] similar.

Differences in the dispersions of [Mg/Fe] and [Ca/Fe] may be partially due to differences in their nucleosynthetic sites, but also may be the result of inhomogeneous mixing of the interstellar gas and therefore poor statistical sampling of the SN contributions when forming stars. In terms of nucleosynthesis, SN yields of Ca and especially Mg depend on the progenitor mass (e.g., Woosley & Weaver 1995; Iwamoto et al. 1999); for example, Mg forms in hydrostatic core C and O burning, whereas Ca has contributions from the α-rich freeze-out and explosive Si burning during the SN II explosion. Differences in the SN Ia models can also lead to differences in the [Si–Ca/Fe] ratios, e.g., the central density, metallicity, ignition source, flame speed, and even type of SN Ia model can play a role (e.g., Maeda et al. 2010; Röpke et al. 2006; Iwamoto et al. 1999). In terms of inhomogeneous mixing, models by Revaz & Jablonka (2012; also Revaz et al. 2009) predict a large spread in the [Mg/Fe] ratios in low-mass dwarf galaxies due to longer gas cooling times and subsequently longer mixing timescales for the ISM. As an example, the hot gas from SNe II can be subject to buoyant forces requiring up to 2 Gyr to cool and mix through a low-mass galaxy. This hot gas can also quench star formation. Therefore, it is possible to find models of low-mass dwarf galaxies that predict both a high dispersion in element ratios and an episodic star formation history, like Carina.

[22] We have estimated the intrinsic spread (N_i) from the formula $N_i^2 = N^2 - \langle\sigma\rangle^2$, where N is the range in [X/Fe] and $\langle\sigma\rangle$ is the average error in [X/Fe].

Surprisingly, the [Mg/Ca] ratios in Carina do not show a larger dispersion then the other dSphs in Figure 20. This may imply that inhomogeneous mixing plays the dominant role (over differences in nucleosynthetic sites). The one star with the extremely low [Mg/Ca] ratio is Car-743, analyzed by Lemasle et al. (2012) from their lowest S/N spectrum; the formal uncertainty in that one result is ∼2× larger than the representative error bar shown, and should be considered with caution. The one star with the highest [Mg/Ca] ratio is Car-1087, analyzed in this paper; with a metallicity of [Fe/H] = −2.9 and high [Mg/Ca] ratio, this star is very similar to the unusual star Draco-119 (discussed below).

5.2.1. Metal-poor Stars and the UFDs

In Figure 21, we show only the metal-poor tail in the Carina abundances and compare the [Mg/Fe] and [Ca/Fe] ratios to those of metal-poor stars in five UFD galaxies and the Draco dSph. Most of the UFD stars have high values of [Mg/Fe] and [Ca/Fe], like the Galactic halo, whereas Carina and Draco show a range extending to very low values.

Some stars in all of these systems show very high [Mg/Ca] values (>0.5), e.g., two stars in the Hercules UFD (Koch et al. 2008b), one in Böotes I (Feltzing et al. 2009), one in Draco (Fulbright et al. 2004; Shetrone et al. 2001), and one in Carina (this paper). In the UFDs, it has been proposed that high [Mg/Ca] may be due to the chemical enrichment of its interstellar gas by as few as one SN II explosion from a massive progenitor (e.g., a $>35\,M_{\odot}$ star). In this scenario, a unique chemical signature can be imprinted onto the gas that is used to form stars, while the rest of the gas is expelled to quench further star formation (e.g., Koch et al. 2008b; Frebel et al. 2010b; Simon et al. 2010). This scenario is aided by peculiar neutron-capture ratios, e.g., in the Hercules stars, the Ba II lines are not detected (Koch et al. 2008b). Similarly, the Ba II (and Sr II) lines in the high [Mg/Ca] star in Draco (Draco-119) are also not detected (Fulbright et al. 2004 suggested that this star was enriched by an SN II in the mass range of 20–25 $M_{\odot}$ and is lacking in contributions from higher mass progenitors). However, Ba II (and Sr II) lines are detected in the high [Mg/Ca] star in Carina. Those lines are weak, leading to very low abundances of [Ba/Fe] and [Sr/Fe], but if the source of these elements is the same as in the other dSphs, then Carina appears to have been able to retain a bit more of those early (high-mass progenitor) SN II enrichments.

5.2.2. Measurement Errors

One question worth considering is whether the large dispersion in [Mg/Fe] is simply due to measurement errors. For example, there are only 1–2 Mg I lines available in each star, whereas there are 3–21 lines of Ca I (depending on the metallicity) in this analysis. Similarly, due to the limited wavelength coverage of the FLAMES/GIRAFFE spectra, there are ⩽13 Ca I lines measured by Lemasle et al. (2012) and only one Mg I line at λ5528. A larger number of spectral lines reduces the random measurement errors in an elemental abundance (by $\sqrt{N}$). This is reflected in the smaller average error in [Ca/Fe] than [Mg/Fe] in Table 10 of Lemasle et al. (2012). In this paper, even if the measurement error from fitting a line is small, as in a high S/N spectrum, the analysis of a single line means that the adopted error is the standard deviation in the Fe I line abundance (σ(Fe); see Section 4.2). These (conservative) errors are about as large as the [Mg/Ca] dispersion, but smaller than the [Mg/Fe] dispersion, therefore the large dispersion in [Mg/Fe] does not appear to be due to measurement errors alone.

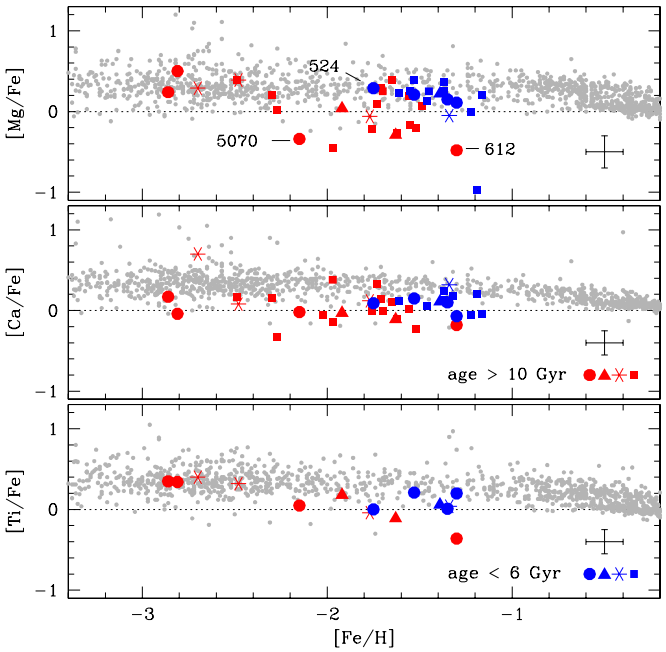

Figure 22. [α/Fe] ratios of stars in the Carina dSph separated into age groups. Symbols are the same as in Figure 20, though now red is used for the old population and blue for the IA population; ages are from Lemasle et al. (2012). Galactic comparison stars are shown as small gray dots (including data from Venn et al. 2004; Frebel et al. 2010b; Reddy et al. 2003, 2006). Representative error bars are shown based on the mean error in the Carina data set.

Another consideration is that variations in the [Mg/Fe] and [Mg/Ca] ratios have been found in a number of metal-poor stars in the UFD galaxies, and attributed to incomplete mixing and poor sampling of the full mass function, as shown in Figure 21. Only the largest outliers are examined in terms of pollution by a single SN II, and similarly large outliers are found in our [Mg/Ca] and [Mg/Fe] data as well. The consistency between these analyses suggests that the signatures in the largest outliers are not due only to measurement errors.

5.3. Age Considerations

The Carina dSph is an interesting galaxy partially because of its low mass and partially because of its episodic star formation history. Lemasle et al. (2012) were the first to attempt to interpret the chemical evolution of this dwarf galaxy after separating the stars into two populations, old (>10 Gyr) and IA (<6 Gyr); stars with ages between 6 and 10 Gyr were examined by Lemasle et al. (2012), but we do not include those in this discussion. The old population shows a large range in [Fe/H] and [Mg/Fe], whereas the IA population appears to have a very small range in [Fe/H] and [Mg/Fe]. Lemasle et al. (2012) were also struck by the significant overlap in [Fe/H] between these populations, which would imply that the IA stars formed from gas that was more metal poor than the end-point metallicity of the old population. Combined with the higher mean [Mg/Fe] abundance of the IA population, Lemasle et al. (2012) suggested that the second epoch of star formation in Carina may have occurred after the late accretion of metal-poor, α-element rich gas.

The overlap in the metallicities of the old and IA population can be seen in Figures 22–24. We note that the overlap is heavily weighted by the age assigned to Car-612, which is the chemically peculiar star discussed in Section 4. Differences in the specific chemistry of stars are known to affect their isochrone ages (Dotter et al. 2007), and thus the age assignment to this star

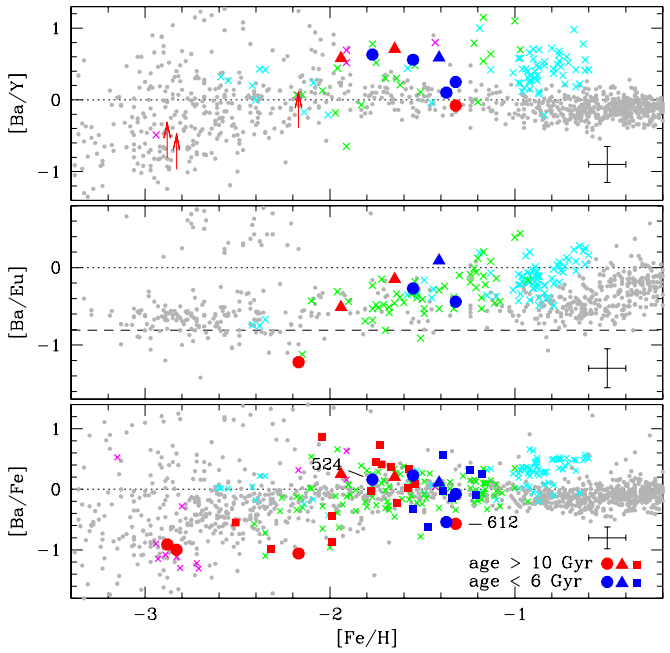

Figure 23. Neutron-capture abundance ratios of stars in the Carina dSph separated into age groups. Data references and symbols for Carina and the Galaxy are the same as in Figure 22. Data for the other dwarf galaxies are noted only by color (cyan for Fornax, green for Sculptor, and magenta for Sextans) with references as in Figure 20.

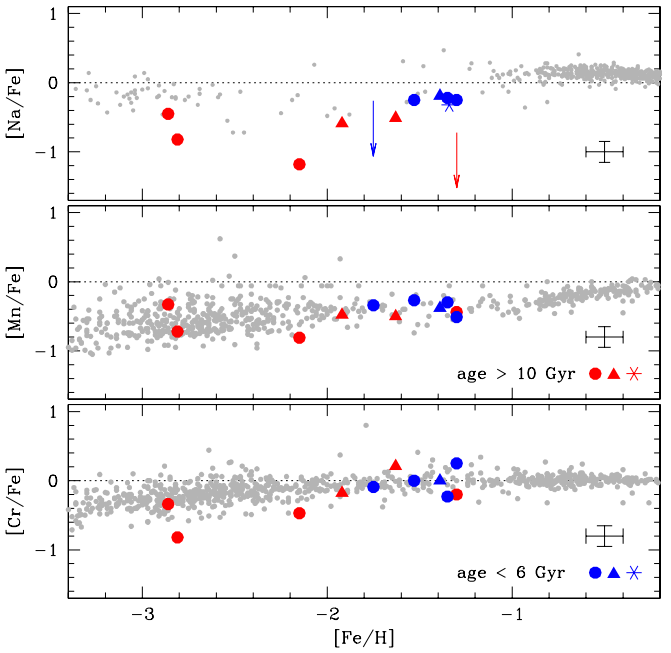

Figure 24. Abundance ratios of [Na/Fe], [Mn/Fe], and [Cr/Fe] for stars in the Carina dSph separated into age groups. Data references and symbols are the same as in Figure 22, with the exception of Na where Galactic data are from Andrievsky et al. (2007), Gehren et al. (2006), Edvardsson et al. (1993), and Reddy et al. (2003, 2006), and also Mn where the Galactic data are from Sobeck et al. (2006) and Cayrel et al. (2004).

should be considered with caution. The overlap is also heavily weighted by Car-524, which has a large uncertainty in its age assignment. If the ages for these two stars are neglected, then there is a sharp transition at $-1.4 < [\mathrm{Fe/H}] < -1.6$ between the age groups, i.e., equivalent to the measurement errors in metallicity. Thus, the overlap in metallicity between the two age groups is not sufficiently clear to indicate an infall of metal-poor gas to form the second generation of stars.

5.3.1. [α/Fe] Ratios Between the Age Groups

An offset in the mean [Mg/Fe] abundance in the IA population relative to the old population can clearly be seen in Figure 22. A Kolmogorov–Smirnov (K-S) test shows that the distribution of the [Mg/Fe] values for the old population is broader and with lower mean values, i.e., $\langle[\mathrm{Mg/Fe}]\rangle_{\mathrm{old}} = 0.05 \pm 0.32$ and $\langle[\mathrm{Mg/Fe}]\rangle_{\mathrm{IA}} = 0.22 \pm 0.15$, both with moderately high probabilities of having "normal" distributions once the outlier in the IA data set (at $[\mathrm{Mg/Fe}] = -0.95$) is removed. This was also seen by Lemasle et al. (2012) for both [Mg/Fe] and [Ca/Fe], although the offset in [Ca/Fe] is not as large, which we confirm with a K-S test. We also note that these offsets in the [Mg/Fe] and [Ca/Fe] ratios with age are still present when only the high-resolution data are examined (this paper; Koch et al. 2008a; Shetrone et al. 2003), although they are not as clear. The same signature is also hinted at in the [Ti/Fe] ratios (from the high-resolution data), but there is insufficient data in the IA population for a meaningful K-S test. Since the large dispersions in the [α/Fe] ratios discussed above (larger than seen in most dSph galaxies) are an indication of inhomogeneous mixing, the simplest explanation for the offset in [α/Fe] between the old and IA population is that the second epoch of star formation occurred in α-enriched gas. The small range in the [α/Fe] and [Fe/H] ratios suggests this gas was well mixed.

5.3.2. The Rise in the s-process

Clearly the old and IA stellar populations in Carina show different chemical signatures, and it is interesting to investigate how the two populations might be connected. While we have discussed the α-elements, possibly the most valuable abundance ratios for studying the chemical evolution of a dwarf galaxy are of the neutron-capture elements.

In Figure 23, it is possible to see that AGB stars have contributed to both age groups in Carina, but not until $[\mathrm{Fe/H}] > -2$. This can be seen by the [Ba/Eu] ratios, where the lower dashed line represents the *r*-process contributions (in the Sun), such that stars with this ratio have been enriched by SNe II products only. Above $[\mathrm{Fe/H}] = -2$, the [Ba/Eu] ratios slowly increase from the low *r*-process value through contributions to Ba from the *s*-process (the *rise* in the *s*-process). This is seen in the Galaxy, Fornax, and Sculptor as well, although the rise begins at higher metallicities in those systems. From the [Ba/Fe] ratios, it is also possible to see how the AGB contributions begin to dominate the nucleosynthesis of Ba, e.g., the dispersion in [Ba/Fe] at low metallicities in the Galaxy is interpreted as the stochastic sampling of the (small amounts of) Ba from SNe II products early on, but this scatter lessens when the dominant contributions from AGB stars come at later times. The flatness of the relationship in [Ba/Fe] at higher metallicities in the Galaxy implies that the timescale and yields of Ba from the AGB stars and Fe from SNe Ia are similar, and the small scatter implies that the gas is well mixed. In Carina, [Ba/Fe] in the IA population may have a large scatter. If the large scatter is real, then this would suggest that the AGB contributions were not well mixed in the ISM at any age, which would be an interesting contrast to the uniformity in the [α/Fe] ratios in the IA population. However, several of these data points are from Lemasle et al. (2012) where the measurements of a single Ba II line were very difficult due to the low S/N in that spectral

region. The data from our high-resolution analysis is far more uniform above [Fe/H] = −2, as shown in Figure 15.

Below [Fe/H] = −2 it is difficult to ascertain whether there are any stars with AGB contributions. There is one star (Car-5070) with [Ba/Eu] below the *r*-process ratio, implying that this star shows no signs of AGB products; however, Carina was poorly mixed at early times, and metal-poor AGB stars could produce very little Ba. The high [Ba/Y] ratios in stars over [Fe/H] = −2 show that most of the *s*-process elements came from metal-poor AGB stars, where the first *s*-process peak (Y) was bypassed in favor of the second *s*-process peak (Ba; as described further in Section 4.4.7)—at even lower metallicities, both can be bypassed for the third *s*-process peak. Therefore, we cannot ascertain the precise metallicity at which AGB stars began to contribute in Carina, but certainly there are contributions from metal-poor AGB stars in the stars with [Fe/H] > −2, and a hint of the rise in the *s*-process between −2.0 < [Fe/H] < −1.6.

Further evidence for the rise in the *s*-process can be seen in the evolution in the [Na/Fe]; see Figure 24. Cayrel et al. (2004) and Andrievsky et al. (2007) showed that the [Na/Mg] and [Na/Fe] ratios are flat and low in metal-poor stars in the Galaxy, suggesting that Na is produced with the α-elements in SNe II at a (low) fixed ratio. The Na abundance rises when AGB stars begin to contribute (see Section 4.4.3). We see a very similar trend in the [Na/Fe] ratios in Carina; in fact, the rise in [Na/Fe] is very similar to the rise in the *s*-process elements. One significant difference though is that the initial [Na/Fe] value appears to be much lower in Carina than in the Galaxy. The final [Na/Fe] ratios may be similar in Carina as in the Galaxy (and Sculptor), and we see no offset in the Na abundances between the old and IA populations. A dispersion in Na is not clear in this small sample.

It is interesting that the evolution of [Mn/Fe] and [Cr/Fe] are also similar to Na in Carina. The abundances of these elements are much lower than in the Galaxy at low metallicities, but then rise above [Fe/H] = −2.0 to abundances that are similar to stars in the Galaxy with the same metallicity. There is also no difference in these elements between the old and IA populations. Like Na, once AGB stars and SNe Ia begin to produce iron-group elements, those contributions will dominate over the initial (low) SNe II yields. The timescale for AGB contributions is thought to be equal to or shorter than that of SNe Ia (∼1 Gyr, Maoz et al. 2010), thus it is likely that both AGB stars and SNe Ia begin to contribute to the ISM in Carina near [Fe/H] = −2.0. The SNe Ia contributions appear to be well mixed in the ISM, and there is no offset between the old and IA stars.

5.3.3. Early Chemical Evolution by SNe II

The earliest stages of chemical evolution in Carina can be examined from the element ratios of the stars below [Fe/H] = −2. As discussed above, these stars appear to have been enriched only in SNe II products. While there is a large range in the [α/Fe] and [Mg/Ca] ratios (when the whole data set is examined, including previously published results), the ratios of Mn, Cr, and Na all start out very low but then rise to the Galactic values at intermediate metallicities.

In addition, the [Sr/Fe] values are among the lowest of all stars analyzed in the Galaxy, other dSphs, and the UFDs (see Figure 25). The [Sr/Fe] values for Car-1087 and Car-7002 are similar to the lowest values found for metal-poor stars in Draco, Boötes I, and Com Ber. Tafelmeyer et al. (2010) suggested that dwarf galaxies may have a lower floor in the [Sr/Fe] ratio

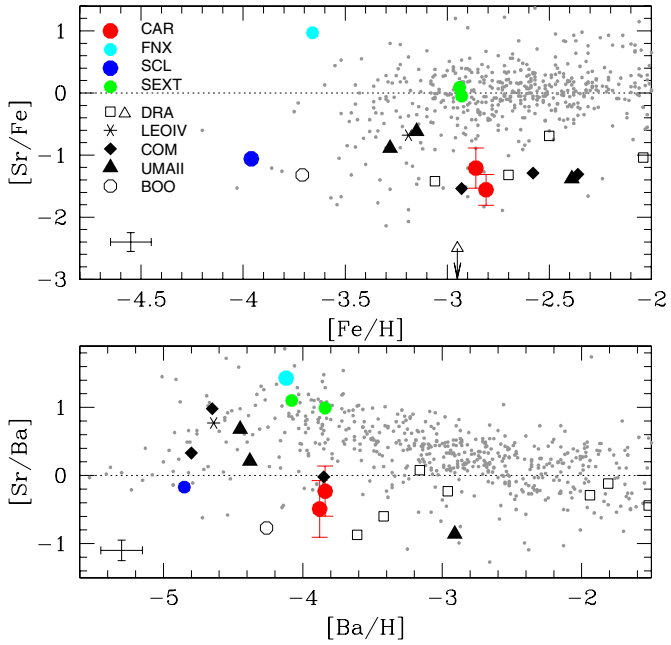

Figure 25. [Sr/Fe] and [Sr/Ba] in low metallicity stars in the Galaxy, classical dSphs, and UFDs. The [Sr/Ba] ratio is enhanced in metal-poor stars in the Galaxy, which is not always seen in the dwarf galaxies. Symbols are the same as in Figure 21.

(∼−1.2) when their mass is equal to or lower than Draco. The low [Sr/Fe] ratios in Carina lead to very low [Sr/Ba] ratios as well. [Sr/Ba] ratios are quite interesting because they tend to be high in metal-poor stars in the Galactic halo, which has been interpreted as evidence for an extra nucleosynthetic source in the formation of these elements in massive stars (Travaglio et al. 2004; Ishimaru et al. 2004; Qian & Wasserburg 2007; Farouqi et al. 2009; Pignatari et al. 2010).

The absence of an [Sr/Ba] enhancement at low metallicities in Carina suggests a *lack* of the excesses seen in the Galactic stars. It is not clear from which stellar mass range these excesses arise: Travaglio et al. (2004) suggest the main *r*-process occurs in 8–10 $M_{\odot}$ stars, and that the excess must arise from the more massive SNe II, whereas Farouqi et al. (2009) suggest the excess occurs in SN II with lower entropy winds where a neutron-rich, α-freezeout can occur. The specific mass or energy range in Farouqi's models is not clear. If we follow Travaglio's suggestions, then the excess Sr may form in more massive, or higher energy SNe II (i.e., hypernovae), and therefore those SNe II seem to be missing in Carina—either those stars did not form or their ejecta was driven out of Carina.[23]

Mn and Cr also form in hypernovae as the decay products of complete and incomplete Si burning (Umeda & Nomoto 2002; Nomoto et al. 2001), thus a lack of hypernovae might also explain the very low initial values of these elements. A neutron-rich, α-freezeout in hypernovae would also contribute to Na production, and thus a lack of hypernovae (i.e., if this is the source of the Sr excess, as in Farouqi et al.'s 2009 models) could explain the very low [Na/Fe] ratios in the most metal-poor

[23] Low upper limits on the [Sr/Fe] and [Ba/Fe] are also reported for Draco-119, however these cannot be used together to constrain [Sr/Ba]. As an exercise, if the upper limits are taken as the actual values, then [Ba/Fe] = −2.6 and [Sr/Ba] = +0.1, which places this star squarely among the Galactic distribution. Thus, even the lack of a detection of the Ba II and Sr II spectra lines in Draco-119 does *not* provide a strong constraint on the one shot hypernova model. The low values *could* be consistent with inhomogeneous mixing and/or gas driven out by supernova winds.

stars. Evolution models (e.g., Salvadori et al. 2008; Brooks et al. 2009, 2007; Ferrara & Tolstoy 2000) suggest that very low mass galaxies can lose gas after the first star-forming epoch through SN II driven winds (possibly reaccreting cold gas for later star formation events). Koch et al. (2006) also suggested that the loss of metal-rich winds would help to explain the metallicity distribution function of Carina, which suffers from the well-known G dwarf problem. Detailed models of the star formation and chemical evolution of Carina by Lanfranchi & Matteucci (2004) invoked two major epochs of outflows through winds. Their best model included a wind efficiency that was 7× the star formation rate and associated with the initial and IA star formation episodes. Thus, the detailed chemical composition of the most metal-poor stars in Carina suggest a lack of hypernovae contributions, possibly implying that these stars did not form, but more likely indicating that their gas was removed from Carina by SN-driven winds.

One alternative to this scenario is that the metal-poor stars are displaying the imprint of the hypernovae, rather than the lack of hypernovae, which would provide a very strong constraint on the nucleosynthetic models. An excellent test of this alternative would be the [Zn/Fe] abundances, which are predicted to be enriched by hypernovae because of an increase in the mass ratio between the complete and incomplete Si-burning regions (Nomoto et al. 2001). We are only able to determine upper limits to the [Zn/Fe] ratios in three stars in Carina below [Fe/H] = −2 from our moderate S/N Magellan/MIKE spectra; however, these limits are tantalizingly close to providing an interesting constraint (see Figure 14). In particular, Car-5070 has a low [Zn/Fe] upper limit and suggests that Car-5070 *lacks* hypernova enrichments.

5.3.4. Summary

Carina and Draco (and possibly Boötes I) appear to be quite different in their early chemical evolution from the other dSphs and UFDs. These two (three) galaxies may be at the critical mass where SN-driven winds remove the gas from the most massive or energetic SNe II progenitors, but the products of the remaining SNe II are retained, and contribute to the (inhomogeneous) chemical evolution of the host. This is unlike the dSphs, which appear to retain the gas from the earliest epochs and undergo a smooth chemical evolution that is not too different from stars in the Galactic halo (other than contributions occurring at lower metallicities, e.g., the AGB yields are from metal-poor stars and the SNe Ia contribute at lower metallicities). Both of these galactic systems are unlike the UFDs, where a single massive SN II may remove all of the gas, quenching the star formation event, and imprinting their unique chemical signatures on the few stars that will complete the star formation process—in this case, any abundance variations within an UFD are due to stochastic sampling of that hypernova and not chemical evolution.

5.4. Car-612: A Pocket of SN Ia Enriched Gas

As discussed in Section 4, Car-612 is underabundant in nearly every element when examined relative to iron, i.e., [X/Fe]. Therefore, we propose that this star is iron enhanced, most likely due to an excess of SN Ia contributions in the gas cloud from which it formed.

In Figure 26, we show the abundance distribution relative to the Galactic averages at [Fe/H] = −1.3 (estimated from the figures in Section 4). Note that very few element ratios lay in the gray band that would describe the [X/Fe] ratios of a typical Galactic star at that metallicity. The only exceptions are Cr, Mn, and Fe, and possibly Si (though the error is large for that element). If this star has an excess of iron by 0.7 dex (a factor of five), then removing this in the [X/Fe] ratios would produce the values in the blue band (other than Fe itself, which we do not adjust). Now Cr, Mn, and Fe (itself) appear enhanced, however nearly all other [X/Fe] ratios are in agreement with the Galactic stars. A direct comparison of spectral line strengths shows that Car-612 has similar Fe I line strengths to stars with similar atmospheric parameters (e.g., Car-705 in Figure 16; also to Car-1013 not shown), while the other lines are weaker.

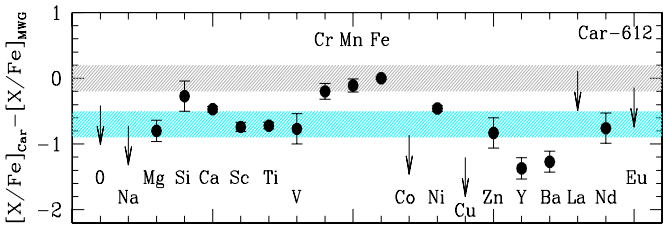

Figure 26. Abundance distribution for Car-612 relative to Galactic stars at its metallicity of [Fe/H] = −1.3. The Galactic abundances are estimated from the distributions in Figures 9–17. The gray shaded area represents a (mean) error in the Galactic abundance of ±0.2 dex. The cyan shaded area represents an offset by −0.7 dex, i.e., if Car-612 were to have a metallicity of −2.0. Note that at [Fe/H] = −2.0, the stars in classical dSphs have similar [X/Fe] values as stars in the Galaxy, thus the apparent iron enrichment does not depend on differences in the chemical evolution of the comparison data set.

(A color version of this figure is available in the online journal.)

This peculiar chemistry makes Car-612 similar to three iron-rich stars in the outer halo, studied by Ivans et al. (2003). These stars are all near [Fe/H] = −2 and have low [α/Fe] ratios, low ratios of Y, Sr, and Ba, and two show enhancements in Cr, Mn, Ni, and Zn. Of those two stars, one is enhanced in Si and Eu. Ivans et al. concluded that these stars have larger SN Ia/II contributions, by factors of 3–7 relative to the average halo star. This is similar to Car-612 where we suggest the enhancement is by a factor of five.

A deep and thorough examination of the predicted yields from existing SN models showed that no combination could reproduce the detailed abundance patterns of the three outer halo stars, i.e., problems remained in the abundances of Ti, Cr, Mn, Ni, and Zn. Since the SN yields are able to reproduce the chemistry of the majority of stars in the Galaxy, Ivans et al. suggested that perhaps the SN yields should not be integrated over a Salpeter initial mass function for these three stars and/or the degree of mixing in the ISM may vary from region to region. If so, they considered that it is also possible for these stars to have been deposited in the outer halo during a dwarf galaxy merger. Variations in their detailed abundances are therefore related to differences in the chemical evolution of their hosts. Car-612 fits with this hypothesis—it appears to be iron-enhanced, and yet its detailed chemistry is again different from that of the three outer halo stars, e.g., Ni, Zn, and Eu are not enhanced. Identifying this star *within* the Carina dwarf galaxy provides additional evidence for inhomogeneous mixing in this low-mass galaxy and provides a clear connection between the formation of these chemically peculiar stars in dwarf galaxies and their existence in the outer Galactic halo.

6. CONCLUSIONS

Carina is an interesting galaxy for chemical evolution studies because of its low mass and its episodic star formation history. In this paper, we have determined the abundances of 23 elements in the spectra of nine RGB stars in the Carina

dSph galaxy taken with both the VLT/FLAMES-UVES and Magellan/MIKE spectrographs. This is a significant increase from the previous number of stars with detailed analyses, e.g., by Shetrone et al. (2003; where all stars had intermediate metallicities) and Koch et al. (2008a; where only the iron and α-element abundances were determined). Our analysis uses both photometric and spectroscopic techniques to determine the stellar parameters, and we use new spherical models, an expanded line list, continuum scattering corrections, and HFS and NLTE corrections (when available) to improve the precision in our abundances. Adopting the ages determined by Lemasle et al. (2012), we are able to examine the chemical evolution of Carina, separating chemical signatures in the old and IA populations. A summary of the most important results in this paper are as follows.

1. *Inhomogeneous mixing.* A large dispersion in [Mg/Fe] indicates poor mixing in the old population. An offset in the [α/Fe] ratios between the old and IA populations (when previously published data are included) also suggests that the second star formation event occurred in α-enriched gas. In addition, one star, Car-612, seems to have formed in a pocket enhanced in SN Ia/II products.
2. *SN-driven winds.* Stars with [Fe/H] < -2 do not appear to have been enriched in AGB or SNe Ia products. Their peculiar chemistry includes very low ratios of [Sr/Ba], an element ratio that usually shows an excess in metal-poor stars in the Galaxy and dSphs. Adopting a scenario where the excess Sr forms in the more massive or energetic SN II, then the lack of this excess in Carina (also Draco and Boötes I) is consistent with the loss of those products by SN II driven winds. Low ratios of [Na/Fe], [Mn/Fe], and [Cr/Fe] support this scenario, with additional evidence from the low [Zn/Fe] upper limit for one star, Car-5070. The α-elements ratios in Car-5070 are also lower than the Galactic distribution.

It is interesting that the chemistry of the metal-poor stars in Carina are not similar to those in the Galaxy, most of the other dSphs, or the UFDs. The [Sr/Fe] and [Sr/Ba] ratios are clear indicators of the differences in the early chemical evolution of these systems: The Galaxy and dSphs appear to retain all of their SN II products and show excesses in the [Sr/Ba] ratios, whereas Carina (with Draco and Boötes I) may be at the critical mass where *some* gas is lost through SN II driven winds, by showing very low [Sr/Fe] and [Sr/Ba] ratios. In the UFDs, all of the gas may be lost with the first SN II, quenching star formation, and imprinting the unique chemical signature of that SN II on the remaining stars as they complete the formation process, thus [Sr/Fe] is low, but [Sr/Ba] can vary.

It is also interesting to find a star with an enhancement in the SN Ia/II products in Carina, similar to the three outer halo stars examined by Ivans et al. (2003). This provides the first direct link between the formation of these stars in low-mass galaxies and their presence in the outer Galactic halo.

We are grateful to the ESO VLT support staff and Magellan support staff for outstanding help and hospitality during our visitor mode observing runs associated with this work. Special thanks to the Stars Group at UVic for our frequent and lively discussions, and help with Magellan/MIKE spectroscopy from Mario Mateo and Andy McWilliam. K.A.V. and M.D. thank NSERC for the Discovery Grant that funded the majority this work. K.A.V. and C.B. thank the NSF for early support through award AST 99-84073.

REFERENCES

Alonso, A., Arribas, S., & Martínez-Roger, C. 1999, A&AS, 139, 335
Alvarez, R., & Plez, B. 1998, A&A, 330, 1109
Andrievsky, S. M., Spite, F., Korotin, S. A., et al. 2011, A&A, 530, A105
Andrievsky, S. M., Spite, M., Korotin, S. A., et al. 2009, A&A, 494, 1083
Andrievsky, S. M., Spite, M., Korotin, S. A., et al. 2007, A&A, 464, 1081
Aoki, W., Arimoto, N., Sadakane, K., et al. 2009, A&A, 502, 569
Aoki, W., Beers, T. C., Christlieb, N., et al. 2007, ApJ, 655, 492
Arlandini, C., Käppeler, F., Wisshak, K., et al. 1999, ApJ, 525, 886
Asplund, M., Grevesse, N., & Sauval, A. J. 2005, in ASP Conf. Ser. 336, Cosmic Abundances as Records of Stellar Evolution and Nucleosynthesis, ed. T. G. Barnes, III & F. N. Bash (San Francisco, CA: ASP), 25
Asplund, M., Grevesse, N., Sauval, A. J., & Scott, P. 2009, ARA&A, 47, 481
Battaglia, G., Irwin, M., Tolstoy, E., et al. 2008, MNRAS, 383, 183
Battaglia, G., Tolstoy, E., Helmi, A., et al. 2006, A&A, 459, 423
Beers, T. C., & Christlieb, N. 2005, ARA&A, 43, 531
Bergemann, M., & Cescutti, G. 2010, A&A, 522, A9
Bergemann, M., & Gehren, T. 2008, A&A, 492, 823
Bergemann, M., Pickering, J. C., & Gehren, T. 2010, MNRAS, 401, 1334
Biehl, D. 1976, PhD thesis, Univ. Kiel
Bono, G., Stetson, P. B., Walker, A. R., et al. 2010, PASP, 122, 651
Booth, A. J., Shallis, M. J., & Wells, M. 1983, MNRAS, 205, 191
Brocato, E., Castellani, V., & Piersimoni, A. 1997, ApJ, 491, 789
Brooks, A. M., Governato, F., Booth, C. M., et al. 2007, ApJ, 655, 17
Brooks, A. M., Governato, F., Quinn, T., Brook, C. B., & Wadsley, J. 2009, ApJ, 694, 396
Brown, J. A., Johnson, H. R., Alexander, D. R., & Wehrse, R. 1987, BAAS, 19, 705
Burris, D. L., Pilachowski, C. A., Armandroff, T. E., et al. 2000, ApJ, 544, 302
Carbon, D. F., Romanishin, W., Langer, G. E., et al. 1982, ApJS, 49, 207
Cayrel, R. 1988, in IAU Symp. 132, The Impact of Very High S/N Spectroscopy on Stellar Physics, ed. G. Cayrel de Strobel & M. Spite (Dordrecht: Kluwer), 345
Cayrel, R., Depagne, E., Spite, M., et al. 2004, A&A, 416, 1117
Cayrel, R., Perrin, M.-N., Barbuy, B., & Buser, R. 1991, A&A, 247, 108
Cohen, J., Christlieb, N., McWilliam, A., et al. 2008, ApJ, 672, 320
Cohen, J., & Huang, W. 2009, ApJ, 701, 1053
Dinescu, D. I., van Altena, W. F., Girard, T. M., & Lopez, C. E. 1999, AJ, 117, 277
Dolphin, A. E. 2002, MNRAS, 332, 91
Dotter, A., Chaboyer, B., Ferguson, J. W., et al. 2007, ApJ, 666, 403
Edvardsson, B., Andersen, J., Gustafsson, B., et al. 1993, A&AS, 102, 603
Fagotto, F., Bressan, A., Bertelli, G., & Chiosi, C. 1994, A&AS, 104, 365
Farouqi, K., Kratz, K. L., Mashonkina, L. I., et al. 2009, ApJ, 694, 49
Feltzing, S., Eriksson, K., Kleyna, J., & Wilkinson, M. I. 2009, A&A, 508, L1
Ferrara, A., & Tolstoy, E. 2000, MNRAS, 313, 291
François, P., Depagne, E., Hill, V., et al. 2007, A&A, 476, 935
Frebel, A. 2010, Astron. Nachr., 331, 474
Frebel, A., Kirby, E., & Simon, J. D. 2010a, Nature, 464, 72
Frebel, A., Simon, J. D., Geha, M., & Willman, B. 2010b, ApJ, 708, 560
Fulbright, J. P. 2000, AJ, 120, 1841
Fulbright, J. P., Rich, R. M., & Castro, S. 2004, ApJ, 612, 447
Gehren, T., Shi, J. R., Zhang, H. W., Zhao, G., & Korn, A. J. 2006, A&A, 451, 1065
Geisler, D., Smith, V. V., Wallerstein, G., Gonzalez, G., & Charbonnel, C. 2005, AJ, 129, 1428
Gratton, R. G., Carretta, E., Bragaglia, A., Lucatello, S., & D'Orazi, V. 2010, A&A, 517, 81
Gratton, R. G., Sneden, C., & Carretta, E. 2004, ARA&A, 42, 385
Gratton, R. G., Sneden, C., Carretta, E., & Bragaglia, A. 2000, A&A, 354, 169
Grevesse, N., & Sauval, A. J. 1998, Space Sci. Rev., 85, 161
Gustafsson, B., Edvardsson, B., Eriksson, K., et al. 2003, in ASP Conf. Ser. 288, Stellar Atmosphere Modeling, ed. I. Hubeny, D. Mihalas, & K. Werner (San Francisco, CA: ASP), 331
Gustafsson, B., Edvardsson, B., Eriksson, K., et al. 2008, A&A, 486, 951
Hambly, N. C., Dufton, P. L., Keenan, F. P., et al. 1994, A&A, 285, 716
Harris, W. E. 1996, AJ, 112, 1487
Heger, A., & Woosley, S. E. 2002, ApJ, 567, 532
Heiter, U., & Eriksson, K. 2006, A&A, 452, 1039
Helmi, A., Irwin, M. J., Tolstoy, E., et al. 2006, ApJ, 651, L121
Hernandez, X., Gilmore, G., & Valls-Gabaud, D. 2000, MNRAS, 317, 831
Herwig, F. 2004, ApJS, 155, 651
Hurley-Keller, D., Mateo, M., & Nemec, J. 1998, AJ, 115, 1840
Irwin, M., & Hatzidimitriou, D. 1995, MNRAS, 277, 1354
Ishimaru, Y., Wanajo, S., Aoki, W., & Ryan, S. G. 2004, ApJ, 600, L47
Ivans, I. I., Sneden, C., James, C. R., et al. 2003, ApJ, 592, 906

Iwamoto, K., Brachwitz, F., Nomoto, K., et al. 1999, ApJS, 125, 439
Karakas, A. 2010, MNRAS, 403, 1413
Karakas, A., Lee, H. Y., Lugaro, M., Görres, J., & Wiescher, M. 2008, ApJ, 676, 1254
Kirby, E. N., Cohen, J. G., Smith, G. H., et al. 2011a, ApJ, 727, 79
Kirby, E. N., Guhathakurta, P., Bolte, M., Sneden, C., & Geha, M. C. 2009, ApJ, 705, 328
Kirby, E. N., Guhathakurta, P., Simon, J. D., et al. 2010, ApJS, 191, 352
Kirby, E. N., Lanfranchi, G. A., Simon, J. D., Cohen, J. G., & Guhathakurta, P. 2011b, ApJ, 727, 78
Kobayashi, C., & Nomoto, K. 2009, ApJ, 707, 1466
Koch, A., Grebel, E. K., Gilmore, G. F., et al. 2008a, AJ, 135, 1580
Koch, A., Grebel, E. K., Wyse, R. F. G., et al. 2006, AJ, 131, 895
Koch, A., McWilliam, A., Grebel, E. K., Zucker, D. B., & Belokurov, V. 2008b, ApJ, 688, 13
Koposov, S., Gilmore, G., Walker, M. G., et al. 2011, ApJ, 736, 146
Lane, R. R., Kiss, L. L., Lewis, G. F., et al. 2009, MNRAS, 400, 917
Lanfranchi, G. A., & Matteucci, F. 2003, MNRAS, 345, 71
Lanfranchi, G. A., & Matteucci, F. 2004, MNRAS, 351, 1338
Lanfranchi, G. A., Matteucci, F., & Cescutti, G. 2006, A&A, 453, 67
Lanfranchi, G. A., Matteucci, F., & Cescutti, G. 2008, A&A, 481, 635
Lawler, J. E., Bonvallet, G., & Sneden, C. 2001a, ApJ, 556, 452
Lawler, J. E., Wickliffe, M. E., den Hartog, E. A., & Sneden, C. 2001b, ApJ, 563, 1075
Lee, J. W., Carney, B. W., & Habgood, M. J. 2005, AJ, 129, 251
Lemasle, B., Hill, V., Tolstoy, E., et al. 2012, A&A, 538, 100
Letarte, B., Chapman, S. C., Collins, M., et al. 2009, MNRAS, 400, 1472
Letarte, B., Hill, V., Jablonka, P., et al. 2006, A&A, 453, 547
Letarte, B., Hill, V., Tolstoy, E., et al. 2010, A&A, 523, 17
Maeda, K., Ropke, F. K., Fink, M., et al. 2010, ApJ, 712, 624
Maoz, D., Sharon, K., & Gal-Yam, A. 2010, ApJ, 722, 1879
Mashonkina, L., Gehren, T., Shi, J., Korn, A., & Grupp, F. 2010, in IAU Symp. 265, Chemical Abundances in the Universe: Connecting First Stars to Planets, ed. K. Cunha, M. Spite, & B. Barbuy (Cambridge: Cambridge Univ. Press), 197
Matteucci, F., Raiteri, C. M., Busso, M., Gallino, R., & Gratton, R. 1993, A&A, 272, 421
McClure, R., Hesser, J. E., Stetson, P. B., Vandenberg, D. A., & Bell, A. R. 1987, AJ, 93, 1144
McWilliam, A. 1998, AJ, 115, 1640
McWilliam, A., Preston, G. W., Sneden, C., & Searle, L. 1995, AJ, 109, 2736
Meynet, G., Ekström, S., & Maeder, A. 2006, A&A, 447, 623
Mighell, K. J. 1997, AJ, 114, 1458
Mishenina, T. V., Kovtyukh, V. V., Soubiran, C., Travaglio, C., & Busso, M. 2002, A&A, 396, 189
Monelli, M., Pulone, L., Corsi, C. E., et al. 2003, AJ, 126, 218
Nakamura, T., Umeda, H., Nomoto, K., Thielemann, F.-K., & Burrows, A. 1999, ApJ, 517, 193
Nissen, P., & Schuster, W. J. 1997, A&A, 326, 751
Nissen, P. E., & Schuster, W. J. 2010, A&A, 511, L10
Nomoto, K., Maeda, K., Umeda, H., & Nakamura, T. 2001, The Influence of Binaries on Stellar Population Studies, Vol. 264 (Dordrecht: Kluwer), 507
Norris, J. E., Gilmore, G., Wyse, R. F. G., et al. 2008, ApJ, 689, L113
Norris, J. E., Wyse, R. F. G., Gilmore, G., et al. 2010a, ApJ, 723, 1632
Norris, J. E., Yong, D., Gilmore, G., & Wyse, R. F. G. 2010b, ApJ, 711, 350
O'Brian, T. R., Wickliffe, M. E., Lawler, J. E., Whaling, W., & Brault, J. W. 1991, J. Opt. Soc. Am. B, 8, 1185
Pasquini, L., Avila, G., Blecha, A., et al. 2002, Messenger, 110, 1
Pietrzyński, G., Górski, M., Gieren, W., et al. 2009, AJ, 138, 459
Pignatari, M., Gallino, R., Heil, M., et al. 2010, ApJ, 710, 1557
Prochaska, J. X., Wolfe, A. M., Tytler, D., et al. 2001, ApJS, 137, 21
Qian, Y.-Z., & Wasserburg, G. J. 2007, Phys. Rep., 442, 237
Ramírez, I., & Meléndez, J. 2005, ApJ, 626, 465
Reddy, B. E., Lambert, D. L., & Allende Prieto, C. 2006, MNRAS, 367, 1329
Reddy, B. E., Tomkin, J., Lambert, D. L., & Allende Prieto, C. 2003, MNRAS, 340, 304
Revaz, Y., & Jablonka, P. 2012, A&A, 538, 82
Revaz, Y., Jablonka, P., Sawala, T., et al. 2009, A&A, 501, 189
Rizzi, L., Held, E. V., Bertelli, G., & Saviane, I. 2003, ApJ, 589, L85
Roederer, I. U., Sneden, C., Thompson, I. B., Preston, G. W., & Shectman, S. A. 2010, ApJ, 711, 573
Röpke, F. K., Hillebrandt, W., & Blinnikov, S. I. 2006, in Beyond Einsten—Physics for the 21st Century, ed. A. M. Cruise & L. Ouwehand (ESA-SP 637; Noordwijk: ESA), 16.1
Salvadori, S., Ferrara, A., & Schneider, R. 2008, MNRAS, 386, 348
Schlegel, D. J., Finkbeiner, D. P., & Davis, M. 1998, ApJ, 500, 525
Shetrone, M. D., Côté, P., & Sargent, W. L. W. 2001, ApJ, 548, 592
Shetrone, M. D., Venn, K. A., Tolstoy, E., et al. 2003, AJ, 125, 684
Short, C. I., & Hauschildt, P. H. 2006, ApJ, 641, 494
Simon, J. D., Frebel, A., McWilliam, A., Kirby, E. N., & Thompson, I. B. 2010, ApJ, 716, 446
Smith, G. H., Briley, M. M., & Harbeck, D. 2005, AJ, 129, 1589
Sneden, C. A. 1973, PhD thesis, Univ. Texas at Austin
Sobeck, J., Frohlich, C., Truran, J., & Kim, Y. 2010, AIP Conf. Ser. 1294, The First Stars and Galaxies: Challenges for the Next Decade, ed. D. J. Whalen, V. Bromm, & N. Yoshida (Melville, NY: AIP), 287
Sobeck, J. S., Ivans, I. I., Simmerer, J. A., et al. 2006, AJ, 131, 2949
Spite, M. 1967, Ann. Astrophys., 30, 685
Starkenburg, E., Hill, V., Tolstoy, E., et al. 2010, A&A, 513, 34
Stetson, P. B. 2000, PASP, 112, 925
Stetson, P. B. 2005, PASP, 117, 563
Stetson, P. B., & Pancino, E. 2008, PASP, 120, 1332
Tafelmeyer, M., Jablonka, P., Hill, V., et al. 2010, A&A, 524, A58
Timmes, F. X., Woosley, S. E., Hartmann, D. H., et al. 1995, ApJ, 449, 204
Tolstoy, E., Hill, V., & Tosi, M. 2009, ARA&A, 47, 371
Tolstoy, E., Irwin, M. J., Helmi, A., et al. 2004, ApJ, 617, L119
Travaglio, C., Gallino, R., Arnone, E., et al. 2004, ApJ, 601, 864
Travaglio, C., Hillebrandt, W., & Reinecke, M. 2005, A&A, 443, 1007
Umeda, H., & Nomoto, K. 2002, ApJ, 565, 385
Umeda, H., & Nomoto, K. 2005, ApJ, 619, 427
Vandenberg, D. A., & Bell, R. A. 1985, ApJS, 58, 561
Venn, K. A., Irwin, M. J., Shetrone, M. D., et al. 2004, AJ, 128, 1177
Walker, M. G., Mateo, M., Olszewski, E. W., et al. 2009, ApJ, 704, 1274
Woosley, S. E., & Weaver, T. A. 1995, ApJS, 101, 181